# **Photo-induced Spatiotemporal Bending of Shape Memory Polymer**

#### **Beams**

Boliang Wu<sup>a</sup>, Tianzhen Liu<sup>a,b</sup>, Yuzhen Chen<sup>a</sup>, Lihua Jin<sup>a,\*</sup>

- Department of Mechanical and Aerospace Engineering, University of California, Los Angeles, Los Angeles, CA 90095, USA
- b. Key Laboratory of C & PC Structures of Ministry of Education, National Prestress Engineering Research Center, Southeast University, Nanjing 210096, China

\*Correspondence: Lihua Jin. Email: <a href="mailto:lihuajin@seas.ucla.edu">lihuajin@seas.ucla.edu</a>

#### **Abstract**

In response to external stimuli, such as heat, light, or magnetic fields, stimuli-responsive soft materials (SRSM) can change their current configuration to a new equilibrium state through nonequilibrium kinetic processes, including reaction, diffusion, and viscoelastic relaxation, which generates novel spatiotemporal shape-morphing behavior. Using a photothermal shape memory polymer (SMP) cantilever beam as a model system, this work analytically, numerically, and experimentally studies its non-equilibrium kinetic processes and spatiotemporal bending under light illumination. We establish a thermomechanical model for SMPs capturing the concurrent non-equilibrium processes of heat transfer and viscoelastic relaxation, which induces inhomogeneous temperature and strain distributions through the thickness of the beam, resulting in its bending and unbending. By varying the key dimensionless parameters, we theoretically and experimentally observe different types of bending dynamics. Moreover, our theory takes into consideration changes in the angles of incidence caused by extensive beam bending, and demonstrates that this effect can dramatically delay the bending due to reduction of the effective light intensity, which is further validated experimentally. This work demonstrates programmable and predictable spatiotemporal morphing of SMPs, and provides design guidelines for SMP morphing structures and robots.

Keywords: Stimuli-responsive material, Shape memory polymer, Spatiotemporal behavior, Non-equilibrium processes, Photothermal-mechanical actuation, Bending dynamics

#### 1 Introduction

Stimuli-responsive soft materials (SRSMs) can change their shapes in response to external stimuli, such as heat, light, magnetic fields, and electric fields [1–3]. For instance, a shape memory polymer (SMP), which is typically a polymer pre-deformed in the rubbery state and cools down to below its glass transition temperature to fix the pre-deformation, can recover its permanent shape when heated above the glass transition temperature [4–7]. A hydrogel, which is a polymer network dispersed in water, can drastically change its volume in response to a change in temperature, light, or pH values [8–10]. SRSMs have shown promising applications in biomedical devices, energy storage, electronic skin, and soft robots [11–15].

In response to external stimuli, SRSMs can change their current configurations to a new equilibrium state through non-equilibrium kinetic processes, including reaction, diffusion, and viscoelastic relaxation. When a SMP is heated above its glass transition temperature, the non-equilibrium kinetics is governed by heat transfer and viscoelastic relaxation [16-18]. In a hydrogel, external stimuli, such as light and pH changes, can induce reactions of the polymer network and diffusion of water molecules [19–22]. The non-equilibrium kinetic processes in SRSMs can often generate inhomogeneous strain inside a material evolving with time, and therefore, novel spatiotemporal shape-morphing behavior [23,24]. A humidity-responsive polymer subjected to a humidity gradient can curl up, and then uncurl or undergo continuous locomotion [25–28]. When a non-equilibrium oscillatory reaction occurs on the polymer network of a hydrogel, the hydrogel can undergo swelling and deswelling oscillation [29,30].

Controlling the response kinetics is a key step to designing programmable SRSMs. In recent years, researchers have developed self-folding structures based on SRSMs [31–33]. The sequential self-folding of an SMP-based composite is achieved by patterning SMPs with different glass transition temperatures and raising the temperature from low to high [31]. Similarly, a photothermal SMP sheet consisting of hinges in different colors sequentially self-folds to a 3D structure attributed to differential light absorption [32]. Structures and robots can also self-actuate

making use of sequential responses of SMPs of different thicknesses to changes in temperature [34,35]. Taking advantage of the fact that deformation of a photo-responsive material can alter its relative orientation to or even block incident light, continuous locomotion and autonomous oscillation have been accomplished in photo-responsive materials [24,36–38], which are further harnessed to achieve bio-mimetic behavior, such as living cilia stir. Moreover, the SRSMs can be 3D-printed into a complex shape, which can further deform in response to external stimuli, namely the 4D printing technique [39–41]. A 3D-printed SMP-based hand and octopus are programmed to exhibit sequential and autonomous bending by manipulating the local temperature and the heating time [40].

Researchers have conducted fundamental studies of the kinetic processes of SRSMs, and predicted their spatiotemporal behavior [23,42–44]. Modeling the diffusion process of water into a paper that contacts with a water bath, researchers are able to predict the curl up of the paper attributed to differential swelling and the uncurl after equilibrium swelling is reached [25]. The kinetic process and spatiotemporal behavior are also studied in a liquid crystal elastomer (LCE), a polymer capable of heating-induced contraction due to a phase transition. The temporal bending and unbending behavior of a thermally responsive LCE cantilever beam subjected to a constant heat source on the boundary is captured by modeling one-dimensional heat conduction through the thickness and the evolution of the heating-induced contraction due to the phase transition [23]. Researchers have extended the kinetic model to take into account a photothermal process, where light absorption generates heat [42]. Moreover, by changing the light intensity, different bending behaviors are observed in the photothermal LCE cantilever [43]. However, the current studies mainly focus on single kinetic process, and only limited work has investigated concurrent kinetic processes [19,45,46]. It is not clear how the coupling of multiple kinetic processes and competition of multiple time scales influence the spatiotemporal behavior of SRSMs. Moreover, the effect of geometry, material, and loading on the spatiotemporal shape-morphing of SRSMs is also less explored.

Using a photothermal SMP cantilever beam as a model system, this work analytically, numerically, and experimentally studies its spatiotemporal bending governed by multiple non-equilibrium kinetic processes, including heat generation, conduction, and viscoelastic relaxation. Through dimensional analysis, we identify the key dimensionless parameters that govern the bending dynamics. By varying the dimensionless parameters that involve multiple kinetic constants, geometry and loading conditions, we observe different types of bending dynamics, which is further experimentally verified. Moreover, using theoretical and experimental methods, we examine the effect of changes in angles of incidence caused by deformation on the spatiotemporal behavior and bending dynamics, and demonstrate that the bending process can be dramatically delayed attributed to reduction of the effective light intensity when a beam subjected to perpendicular illumination bends significantly. This work demonstrates a generic method of studying the spatiotemporal behavior of SRSMs governed by multiple concurrent non-equilibrium processes and provides design guidelines for programmable and predictable spatiotemporal morphing structures and robots.

The paper is organized as follows. Section 2 describes the finite element analysis of the thermomechanical cycle of a SMP cantilever beam, and its bending dynamics under light illumination. We discover three different types of bending dynamics. Section 3 presents an analytical model of bending dynamics involving the kinetic processes of photothermal heat generation, conduction, and viscoelastic relaxation. Section 4 discusses dimensional analysis, and the effect of the key dimensionless parameters on the spatiotemporal behavior and bending dynamics of the SMP beam. Section 5 demonstrates the effect of changes in angles of incidence on the bending dynamics. In Section 6, we experimentally verify the three types of bending dynamic behavior and the effect of changes angles of incidence. Section 7 concludes the paper.

## 2 Finite element analysis and three types of bending dynamics

Here we load and actuate a SMP beam through a thermomechanical cycle (figure 1). (i)

Initially, the beam with a length  $l_0$  is uniaxially deformed to a specific pre-stretch,  $\varepsilon_{pre}$ , above its glass transition temperature  $(T_g)$ . (ii) Afterwards the beam is cooled to ambient temperature  $T_0$ , which is below  $T_g$ , under the same strain. (iii) Then the strain is unloaded at the same temperature. As a result, only a small amount of strain recovers, leaving the length of the SMP L, and the stored strain  $\varepsilon_s$  fixed in the sample. (iv) Finally, shape recovery is achieved by reheating (by stimuli) the beam to above  $T_g$  without any loading constraint. The stored strain is released, and the beam can recover its initial state. The schematics of the SMP beam in the thermomechanical cycle is illustrated in figure 1(a), while the homogeneous stress-strain history is shown in figure 1(b).

However, the deformation of the SMP in the recovery step can be highly inhomogeneous, governed by kinetic processes, in response to external stimuli, specifically light illumination. When light is illuminated from one side of the SMP beam, the light intensity decays due to absorption, which generates heat (figure 2(a)). The heat is conducted in the beam and gets lost on the boundaries to the ambient at temperature  $T_0$ . Since the releasing of the stored pre-stretch is a viscoelastic process with the viscosity strongly depending on the temperature, a temperature gradient in the sample can generate inhomogeneous strain through the thickness of the beam and result in bending (figure 2(b)). If the temperature in the entire sample reaches above  $T_g$ , the deformation everywhere fully recovers, and the sample unbends.

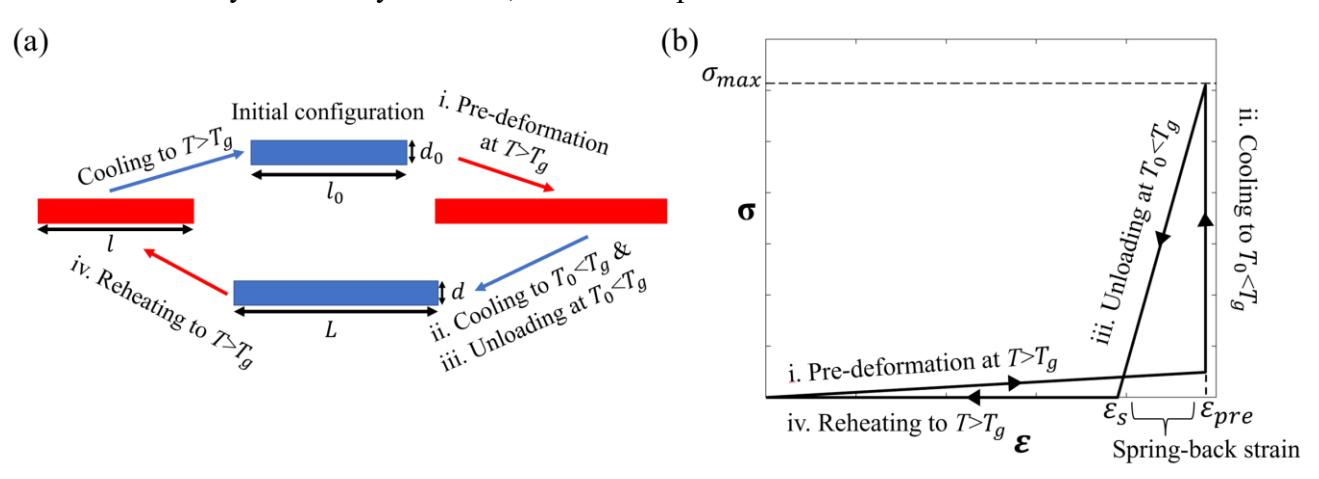


Figure 1 (a) Schematic of the thermomechanical cycle of a SMP beam, and (b) the corresponding homogeneous stress-strain history.

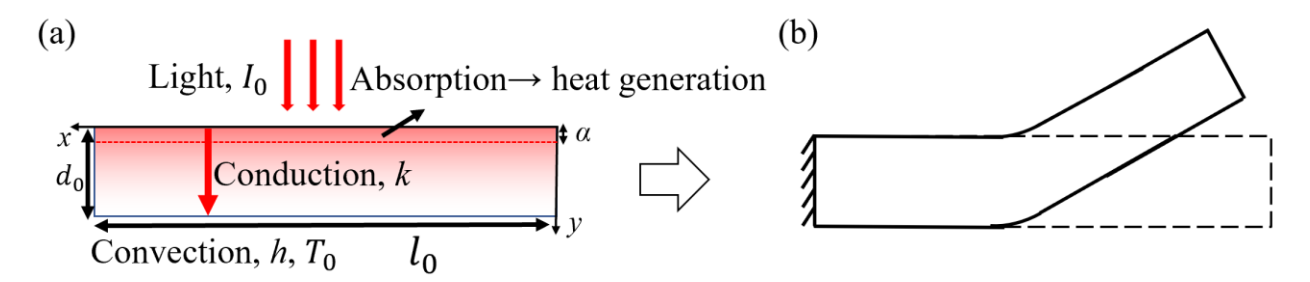


Figure 2 Schematic of (a) light absorption, heat generation, conduction, and convection in a SMP beam in the initial undeformed configuration, and (b) its temporal bending behavior governed by non-equilibrium processes.

We conduct finite element analysis (FEA) combining thermomechanically coupled elements that can capture the above mentioned kinetic processes of heat transfer, in conjunction with a viscoelastic material model, where both the modulus and viscosity are strong functions of temperature, to predict the spatiotemporal bending of photothermal SMP cantilever beams using commercial software ABAQUS/Standard 6.14.

The Poisson's ratio v of the SMP is assumed to be a constant, while the instantaneous Young's modulus  $E_0$  is modeled as a function of temperature T by [47,48]

$$E_0(T) = E_l + \frac{E_h - E_l}{1 + e^{0.3 \cdot (T - T_g)}},\tag{1.}$$

where  $E_h$  and  $E_l$  are, respectively, the moduli at high and low temperature, between which the modulus undergoes a sharp transition at  $T = T_g$ . The rheological model is chosen to be the standard linear solid (SLS) (figure 3), which consists of a single spring element with a modulus  $E_0(1-g)$ , and a spring-dashpot element in parallel with the modulus of the spring  $E_0g$  and viscosity of the dashpot  $\eta a$ , with g the relaxation factor. As a result, the instantaneous modulus of the SMP is  $E_0$ , while the long-term modulus drops to  $E_0(1-g)$ . The shifting factor a as a function of temperature T, a(T), accounts for the time-temperature superposition modeled by William-Landel-Ferry (WLF) function [49],

$$a(t) = 10^{\frac{-C_1(T - T_g)}{C_2 + (T - T_g)}},$$
(2.)

where  $C_1 = 17.44$  and  $C_2 = 51.6$  K are empirical constants. Therefore, the effective modulus of the SMP under a constant strain as a function of temperature T and time t can be written as

$$E(T,t) = E_0(T) \left( 1 - g \left( 1 - e^{-\frac{t}{\tau(T)}} \right) \right), \tau(T) = \frac{\eta a(T)}{gE_0(T)},$$
 (3.)

with  $\tau$  is the relaxation time scale.

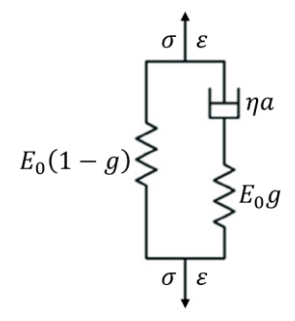


Figure 3 SLS model used to describe the viscoelastic behavior of SMPs.

We consider uniform light illumination along the length direction on the top of the beam (figure 2(a)). Through the thickness, the light propagation is assumed to satisfy the Beer-Lambert law with an absorption decay length  $\alpha$  [42,43]. Due to the photothermal effect, heat is generated inside the beam by absorbing the light. Thus, the volumetric heat generation rate due to light absorption is modeled as

$$Q(y) = -\frac{\partial I_{\lambda_0}}{\partial y} = \frac{I_0}{\alpha} e^{-\frac{y}{\alpha}},\tag{4.}$$

where  $I_0$  is the initial light intensity, and y is the coordinate along the thickness direction in the initial undeformed state. Meanwhile, the generated heat conducts with a thermal conductivity k and volumetric heat capacity  $C_v$ , and lost on all the boundaries to the ambient at lower temperature  $T_0$  with a convection coefficient h (figure 2(a)). The two-dimensional heat equation is solved in conjunction with the viscoelastic stress equilibrium equation using the coupled temperature-displacement step and 8-node plane strain thermally coupled quadrilateral element CPE8T in ABAQUS to determine the spatiotemporal behavior of the SMP cantilever. In the next section the one-dimensional heat equation and boundary condition are listed as equations (10) and (11), and

will be solved numerically together with a beam model to analytically determine the bending dynamics of SMP cantilevers.

In the following simulations in this section, we will set the parameters as:  $E_h = 10$  MPa,  $E_l = 125$  MPa, v = 0.33, g = 0.8,  $T_g = 333$  K,  $\tau(T_g) = 0.1$  s,  $\alpha = 60$  µm,  $C_v = 1.3 \times 10^6$  Jm<sup>-3</sup>K<sup>-1</sup>, k = 0.35 Wm<sup>-1</sup>K<sup>-1</sup>, h = 25 Wm<sup>-2</sup>K<sup>-1</sup>, and  $T_0 = 293$  K.

Before studying the bending dynamics of a photothermal SMP beam undergoing the full thermomechanical cycle accounting for the kinetics of heat transfer, we first compute the uniform stored strain  $\varepsilon_s$  in the recovery step resulted from the first three steps in the cycle under the assumption of homogeneous temperature and deformation. Since we do not consider the heat transfer process, we just simply use the 4-node bilinear plane strain quadrilateral element CPE4R by assuming uniform distribution of temperature inside the beam. Structure elements with an aspect ratio close to 1 are used to mesh the SMP beam, and a minimum of 20 elements are used along the thickness. The time increment is selected to be close to the viscoelastic time scale  $\tau(T_g)$ and checked against convergence. A SMP beam of length  $l_0 = 10 \text{ mm}$  and thickness  $d_0 = 1 \text{ mm}$ is pre-stretched to  $\varepsilon_{pre}$  = 5%, 10%, 15% strain at T = 353 K (figure 1(a)). Then the temperature is cooled from 353 K to 293 K with a constant rate - 0.75 Ks<sup>-1</sup> prior to removing the load. Finally, the temperature increases from 293 K to T with a constant rate of 0.75 Ks<sup>-1</sup>. The stored strain as a function of time t, and therefore temperature T,  $\varepsilon_s(T)$ , in the recovery step is computed (figure 4). The result shows that at a temperature lower than  $T_g$  most strain is stored with a small springback from  $\varepsilon_{pre}$  after removing the load, while as the temperature increases, the stored strain decreases dramatically and completely recovers zero at a temperature slightly higher than  $T_q$ .

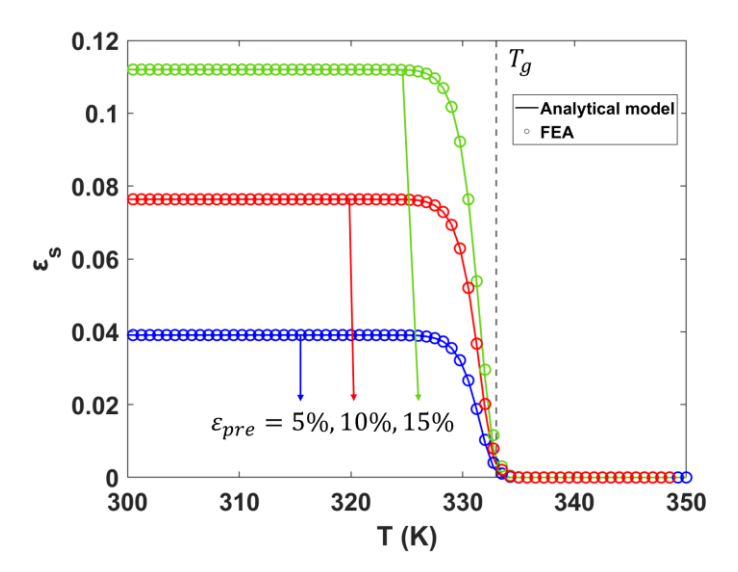


Figure 4 Comparison of the results from FEA and analytical model on the relation between the stored strain  $\varepsilon_s$  and temperature under pre-stretch  $\varepsilon_{pre} = 5\%$ , 10%, and 15% with a constant heating rate of 0.75 Ks<sup>-1</sup>.

Next, we use the 8-node plane strain thermally coupled quadrilateral element CPE8T to capture the bending and unbending phenomenon in the recovery step after a full thermomechanical cycle accounting for the kinetics of heat transfer. A structure mesh similar to that described in the last paragraph is used. To accurately capture the solution to the heat equation, the time increment is selected to be close to the diffusion time scale across an element,  $C_v m^2/k$  with m the element size, and checked against convergence. The loading in the first three steps are the same as described in the last paragraph. In the recovery step, the temperature and strain in the photothermal SMP in response to light illumination can be highly inhomogeneous, governed by kinetic processes (figure 5). A SMP beam with the same dimension as the previous case is first uniaxially pre-stretched to 5% strain at T = 353 K (figure 5(a) and (b)), and then cooled to 293 K to fix the deformed shape (figure 5(c)). When the SMP beam is illuminated by light with intensity  $I_0 = 3000$  Wm<sup>-2</sup> from the top surface, the top layers absorb light and convert it to heat, which is gradually conducted into the bottom layer or lost on the boundaries. Figure 5(c) shows the temporal evolution of the temperature at different locations  $y/d_0 = 0$ , 0.5, 1, which corresponds to the top, middle and bottom surfaces, respectively. The temperature at different locations gradually increases to above

 $T_g$ , but the temperature on the top surface is always higher than that on the bottom surface. Once the temperature reaches  $T_g$ , the stored pre-stretch  $\varepsilon_s$  is released. The stored strain on the top surface is released earlier than that in other places (figure 5(f)), leading to a significant strain gradient through the thickness, which causes bending of the beam (figure 5(d)). When the temperature in the entire sample reaches above  $T_g$ , the stored strain becomes zero everywhere, and the sample unbends. Correspondingly, the bending curvature R normalized by the initial thickness of the beam (figure 1(a)),  $d_0/R$ , non-monotonically increases and then decreases to zero (figure 6(b)).

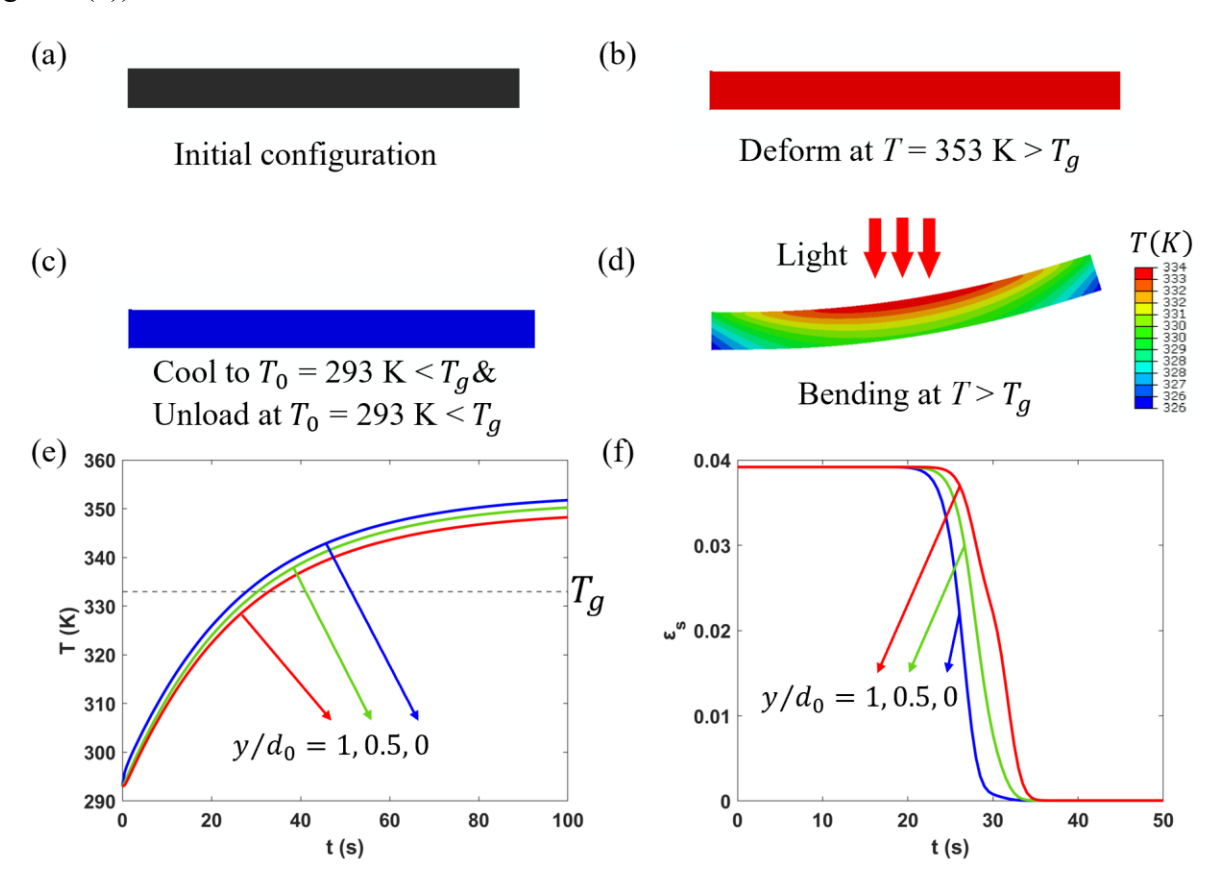


Figure 5 FEA results showing the (a) initial configuration, (b) pre-deformed shape, (c) cooling and unloading processes, (d) and bending of a SMP beam at t = 29.3 s. The color in part (d) represents the temperature distribution. Temporal evolution of the (e) temperature and (f) stored strain at  $y/d_0 = 0, 0.5, 1$  from the FEA.

We next demonstrate three different types of bending dynamics by simply varying the light intensity from  $I_0 = 3000$  Wm<sup>-2</sup>, 2000 Wm<sup>-2</sup> to 1750 Wm<sup>-2</sup> (figure 6, see Supplementary video S1). The three types of bending dynamics are similar to that predicted by Zhou et al. [43]. When  $I_0 = 3000$  Wm<sup>-2</sup>, the temperature on the top and bottom surfaces of the SMP gradually increases to above  $T_g$  (figure 6(a)). Correspondingly, the normalized bending curvature,  $d_0/R$ , of the SMP increases, reaches the maximum value, and gradually decreases to zero (figure 6(b),). When the light intensity is lower,  $I_0 = 2000$  Wm<sup>-2</sup>, the temperature on the top surface of the SMP gradually increases to above  $T_g$  but the temperature on the bottom surface reaches a plateau value below  $T_g$  due to the heat loss by convection (figure 6(a)). As a result, the curvature nonmonotonically increases and decreases, but eventually reaches a non-zero plateau value (figure 6(b)). The beam does not completely unbend, but remains in a bent state. When the light intensity is very low,  $I_0 = 1750~\mathrm{Wm^{-2}}$ , the temperature on the top and bottom surfaces of the SMP are much lower than  $T_g$  (figure 6(a)), and the bending curvature monotonically increases until a plateau value (figure 6(b)). In the following sections, we will further develop an analytic model and conduct experiments to better understand how the coupling and competition of multiple kinetic processes influences the bending dynamics.

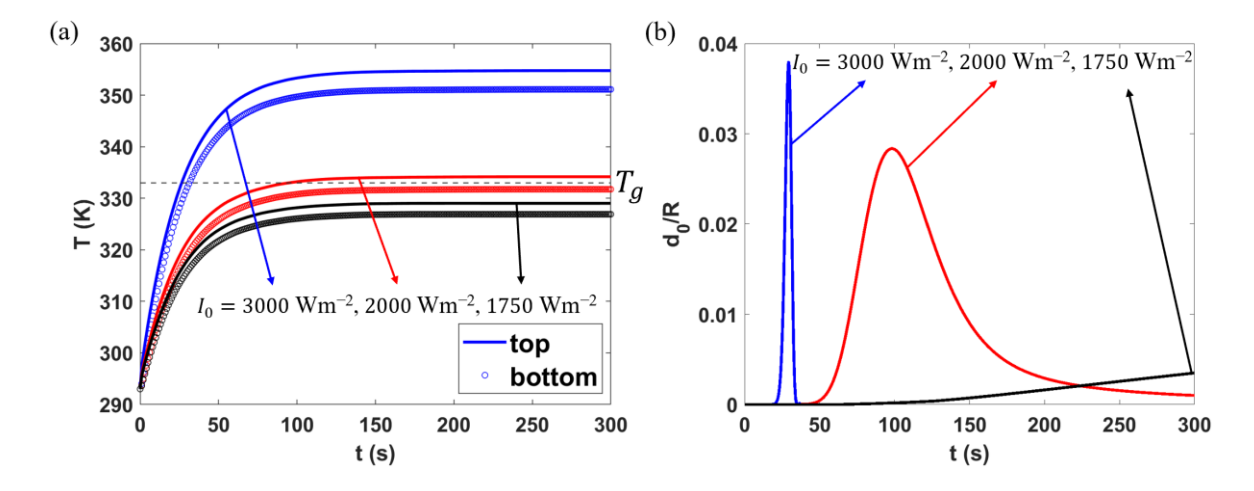


Figure 6 (a) Temporal evolution of the temperature on the top and bottom surfaces of the SMP beam under light intensity  $I_0 = 3000 \text{ Wm}^{-2}$ , 2000 Wm<sup>-2</sup> and 1750 Wm<sup>-2</sup>. (b) The temporal evolution of the bending curvature shows three different types of bending behavior for the three

light intensities.

### 3 Theoretical model

In this section, to better understand the bending dynamics we establish an analytical model, which also facilitates the dimensional analysis in the later section. To model the bending behavior of the SMP beam due to differential recovery of the stored strain through the thickness, we will first model uniform shrinkage of the SMP beam to investigate the relation between the stored strain and temperature. Then, we will establish a dynamic bending model for the photothermal SMP cantilever beam accounting for its multiple kinetic processes, and compare the results with FEA simulations.

#### 3.1 Uniform contraction

In this section, we will first model uniform contraction, where the temperature is assumed distributed uniformly in the SMP beam. Same as that in the FEA, the SMP beam is uniaxially prestretched to a specific strain  $\varepsilon_{pre}$  above its  $T_g$ . Then the beam is cooled to  $T_0 < T_g$  under the same strain. Next, the load is removed, and the stored strain  $\varepsilon_s$  is fixed in the beam. Finally, when the sample is heated again, the stored strain further evolves as a function of time,  $\varepsilon_s(t)$ .

Here we also adopt the SLS model for the SMP (figure 3). It assumes that the total stress  $\sigma$  equals the summation of those on the single spring and spring-dashpot elements, while both the elements have the same total strain  $\varepsilon$ , which equals the summation of the strains in the spring and dashpot in the spring-dashpot element. Based on the above assumptions, we can obtain the relation between the stress  $\sigma$  and strain  $\varepsilon$ ,

$$\sigma + \frac{\eta a}{gE_0}\dot{\sigma} = E_0(1-g)\varepsilon + \frac{\eta a}{g}\dot{\varepsilon},\tag{5.}$$

where  $\dot{\sigma}$  is the changing rate of the stress, and  $\dot{\varepsilon}$  is the changing rate of the strain. Based on the thermomechanical cycle, the stored strain in the recovery step is released without any stress.

Therefore, we have

$$\dot{\sigma} = 0, \sigma = 0, \varepsilon = \varepsilon_{s} \tag{6.}$$

and equation (5) can be further simplified to

$$E_0(T)(1-g)\varepsilon_s + \frac{\eta a(T)}{g}\dot{\varepsilon_s} = 0, \tag{7.}$$

The recovery of the stored strain as a function of time,  $\varepsilon_s(t)$ , can be obtained by solving equation (7) with a prescribed heating rate, T = T(t), inserted into the temperature-dependent  $E_0(T)$  and a(T). Specifically, in this subsection we consider a constant heating rate,  $T(t) = T_0 + \dot{T}t$ . The initial condition of  $\varepsilon_s$  at the beginning of the recovery step, t = 0, can be obtained by calculating the spring-back strain due to removal of the load (figure 1(b))

$$\varepsilon_s(0) = \varepsilon_{pre} - \frac{\sigma_{max}}{E_l},\tag{8.}$$

where  $\sigma_{max}$  represents the peak stress after cooling, and can be determined by solving equation (5) at the end of the cooling step, i.e. setting  $\dot{\sigma} = 0$ ,  $\dot{\varepsilon} = 0$ ,  $\varepsilon = \varepsilon_{pre}$  and  $T = T_0$ 

$$\sigma_{max} = E_0(T_0)(1 - g)\varepsilon_{pre},\tag{9.}$$

Hence, by solving  $\varepsilon_s(t)$  using equations (7)-(9) and inserting the temperature-time relation T(t) into  $\varepsilon_s(t)$ , we can obtain the relation between the stored strain and temperature  $\varepsilon_s(T)$ . All the parameters, including the heating rate  $\dot{T}$ , are selected to be the same as the FEA. The dependence of the stored strain on temperature from the analytical results agrees well with that from FEA (figure 4). When increasing the heating rate from  $\dot{T} = 0.01 \text{ Ks}^{-1}$ , 0.75 Ks<sup>-1</sup>, 22 Ks<sup>-1</sup> to 10000 Ks<sup>-1</sup>, we can see a higher heating rate delays the releasing of stored strains at the same temperature (figure 7). But eventually, at a high enough temperature, the stored strain can fully recover.

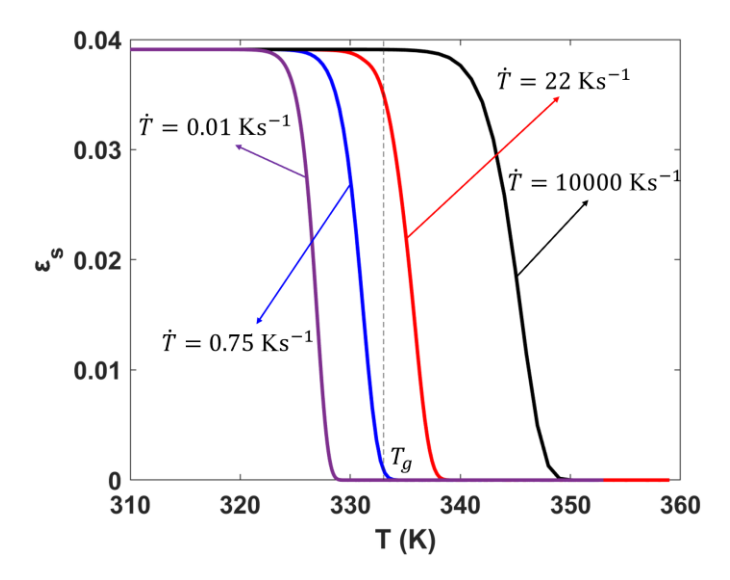


Figure 7 The results from the analytical model on the relation of stored strain  $\varepsilon_s$  and temperature T for a SMP subjected to pre-stretch  $\varepsilon_{pre} = 5\%$  and different heating rate  $\dot{T} = 0.01~{\rm Ks}^{-1}$ , 0.75 Ks<sup>-1</sup>, 22 Ks<sup>-1</sup> and 10000 Ks<sup>-1</sup>.

### 3.2 Bending

In this section, we will consider the recovering step of the SMP beam subjected to light illumination, where heat generates and conducts through the thickness of the beam, and the generated temperature gradient gives rise to differential strain and bending behavior. Assuming that the light is uniformly distributed along the length direction and only propagates through the thickness direction of the SMP beam, we can simplify the heat equation to a one-dimensional problem along the thickness direction *y*,

$$C_{v} \frac{\partial T(y,t)}{\partial t} - k \frac{\partial^{2} T(y,t)}{\partial y^{2}} = Q(y), \qquad (10.)$$

where the temperature T(y,t) is a function of position y and time t, the thermal conductivity k and volumetric heat capacity  $C_v$  are the same as defined in Section 2, and the volumetric heat generation rate Q(y) is defined in equation (4). Thus, the stored strain  $\varepsilon_s(T,t)$  and modulus E(T,t) become functions of position and time,  $\varepsilon_s(y,t)$  and E(y,t). The generated heat gets lost on the top and bottom boundaries to the ambient at temperature  $T_0$ , so the boundary conditions are

$$-k\frac{\partial T}{\partial y} = -h(T - T_0) \text{ at } y = 0, -k\frac{\partial T}{\partial y} = h(T - T_0) \text{ at } y = d_0.$$
 (11.)

Taking the deformed shape at the beginning of the recovery step as the reference state, we define the light-induced strain as

$$\varepsilon_L(y,t) = \frac{l(y,t)}{L(y)} - 1, \tag{12.}$$

where  $L(y) = (1 + \varepsilon_s(y, 0)) \cdot l_0$  is the initial length in the reference state, and the current length is  $l(y, t) = (1 + \varepsilon_s(y, t)) \cdot l_0$ . The light-induced strain can be written as

$$\varepsilon_L(y, t) = \frac{\varepsilon_S(y, t) - \varepsilon_S(y, 0)}{1 + \varepsilon_S(y, 0)}.$$
 (13.)

The total strain is composed of light-induced strain  $\varepsilon_L(y, t)$  and elastic strain  $\varepsilon_e(y, t)$  [50]

$$\varepsilon(y,t) = \varepsilon_L(y,t) + \varepsilon_e(y,t). \tag{14.}$$

Assuming the strain is small and the simple beam theory is applicable, we obtain the relation between the radius of curvature of the neutral plane, R, and the strain difference at y and the neutral plane  $y_n$ ,  $\varepsilon(y,t) - \varepsilon(y_n,t)$ ,

$$\varepsilon(y,t) - \varepsilon(y_n,t) = \frac{y - y_n}{R(t)}.$$
 (15.)

Since there is no stress at the neutral axis, we have  $\varepsilon_e(y_n, t) = 0$ , and thus

$$\varepsilon(y_n, t) = \varepsilon_L(y_n, t). \tag{16.}$$

Combining equations (14)-(16), we obtain

$$\varepsilon(y,t) = \frac{y - y_n}{R(t)} + \varepsilon_L(y_n, t), \tag{17.}$$

$$\varepsilon_e(y,t) = \frac{y - y_n}{R(t)} + \varepsilon_L(y_n,t) - \varepsilon_L(y,t), \tag{18.}$$

and the stress is

$$\sigma(y,t) = E\varepsilon_e = E(y,t) \left[ \frac{y - y_n}{R(t)} + \varepsilon_L(y_n,t) - \varepsilon_L(y,t) \right]. \tag{19.}$$

Since there is no external force or moment, the force and moment balance should be satisfied

$$N = \int_0^{d_0} \sigma \, dy = 0 \quad and \quad M = \int_0^{d_0} \sigma y \, dy = 0. \tag{20.}$$

By plugging equation (19) into equation (20) and eliminating  $\varepsilon_L(y_n, t) - y_n/R$ , we can obtain

the evolution of the dimensionless curvature  $d_0/R(t)$  as

$$\frac{d_0}{R(t)} = \frac{E^1 \overline{\sigma_L} - \frac{E^0 \overline{m_L}}{d_0}}{E^{1^2} - E^0 E^2},\tag{21.}$$

where 
$$E^0 = \frac{1}{d_0} \int_0^{d_0} E \, dy$$
,  $E^1 = \frac{1}{{d_0}^2} \int_0^{d_0} E y \, dy$ ,  $E^2 = \frac{1}{{d_0}^3} \int_0^{d_0} E y^2 \, dy$ ,  $\overline{\sigma_L} = \frac{1}{d_0} \int_0^{d_0} E \varepsilon_L \, dy$ ,  $\overline{m_L} = \frac{1}{d_0} \int_0^{d_0} E \varepsilon_L y \, dy$ .

We use the following algorithm to determine the temporal evolution of the radius of curvature, R(t), solved in MATLAB. The partial differential equation (10) is first solved by the function Pdepe to determine the spatiotemporal distribution of temperature T(y,t). Then the stored strain  $\varepsilon_s(y,t)$  at a given position y as a function of time t is solved from the ordinary differential equation (7) via the function Ode45 with the heating history T(y,t) obtained in the previous step. Next,  $\varepsilon_L(y,t)$  is obtained from equation (13). Finally, R(t) is determined by equation (21).

The same parameters in the FEA shown in figure 5 are used in the theoretical model to compare the results. Figure 8(a) shows that the temporal evolution of the temperature at different locations from the analytical model is almost the same as the FEA results shown in figure 5(e). Figure 8(b) shows the temporal evolution of the light-induced strain  $\varepsilon_L$ , which undergoes a sharp transition from zero to a negative value at different time for points at different locations  $y/d_0$ , leading to differential strain through the thickness, and therefore, bending of the beam. The bending curvature calculated using equation (21) increases, reaches the maximum value, and then decreases with time, showing a similar trend as that in FEA (figure 8(c)). However, the value slightly deviates from that in the FEA, potentially because the stored strain  $\varepsilon_s(y,t)$  obtained as described in Section 3.1 is at zero stress, which is violated in the two-dimensional FEA.

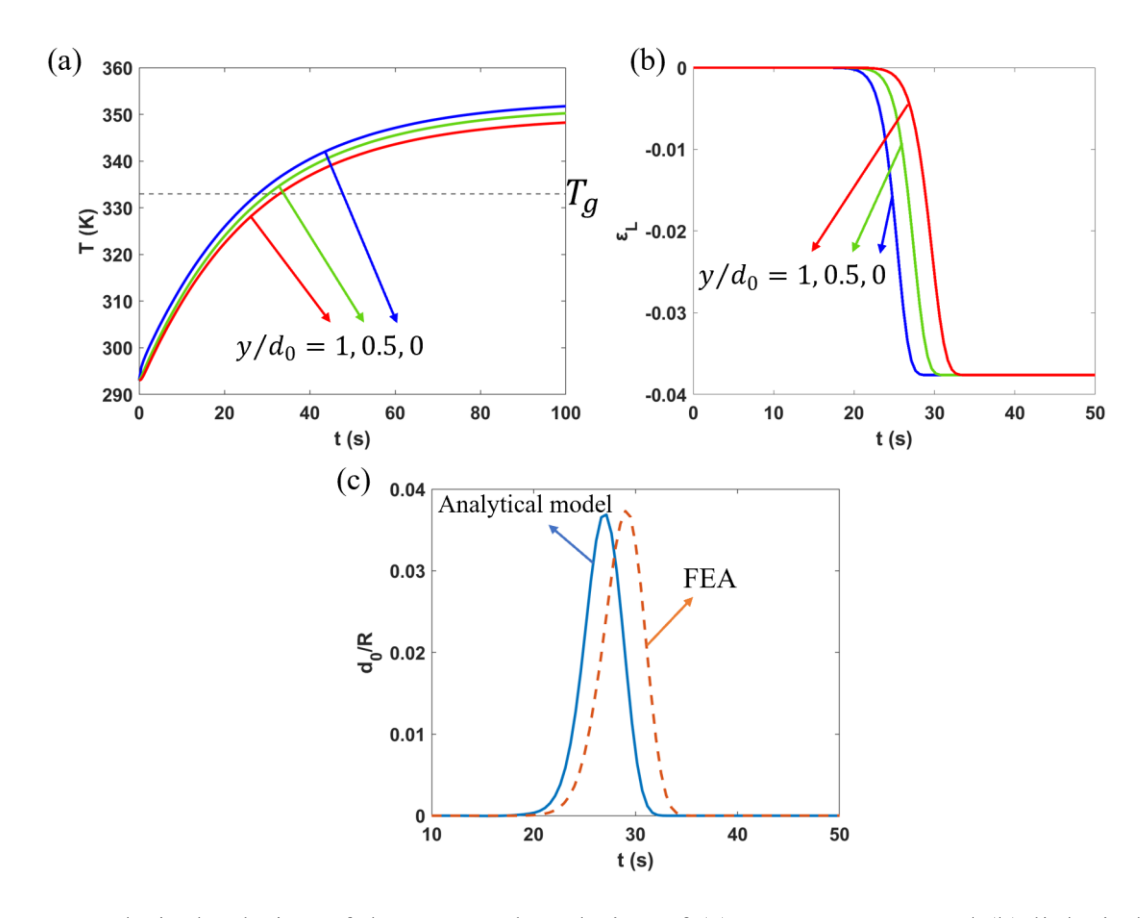


Figure 8 Analytical solution of the temporal evolution of (a) temperature T and (b) light-induced strain  $\varepsilon_L$  at  $y/d_0 = 0, 0.5, 1$ . (c) Comparison of the temporal evolution of the curvature from the analytical model and FEA.

#### 4 Dimensional analysis

The non-equilibrium processes, including heat transfer and viscoelastic relaxation, determine the spatiotemporal temperature and strain distributions, and therefore the bending dynamics, of the SMP beam. To investigate the influence of geometry and material properties, including the kinetic constants of the multiple kinetic processes, on the bending dynamics, dimensional analysis will be conducted in this section.

We normalize all the equations. In particular, the heat equation and its boundary conditions, equations (10) and (11) in Section 3 are normalized as

$$\frac{\partial \hat{T}}{\partial \hat{t}} - \frac{\partial^2 \hat{T}}{\partial \hat{v}^2} = \hat{I}e^{-\frac{\hat{v}}{\hat{\alpha}}},\tag{22.}$$

$$\frac{\partial \hat{T}}{\partial \hat{y}} = \hat{h}(\hat{T} - 1) \text{ at } \hat{y} = 0, -\frac{\partial \hat{T}}{\partial \hat{y}} = \hat{h}(\hat{T} - 1) \text{ at } \hat{y} = 1, \tag{23}$$

where

$$\hat{T} = \frac{T}{T_0}, \hat{t} = \frac{tk}{C_v d_0^2}, \hat{y} = \frac{y}{d_0}.$$
 (24)

There are totally ten dimensionless numbers in this coupled thermomechanical problem defined as

$$\hat{I} = \frac{I_0 d_0^2}{k T_0 \alpha}, \hat{\alpha} = \frac{\alpha}{d_0}, \hat{h} = \frac{h d_0}{k}, g, \varepsilon_{pre}, \tag{25}$$

$$\pi_1 = \frac{E_l}{T_0 C_v}, \pi_2 = \frac{\eta k}{E_l C_v d_0^2}, \pi_3 = \frac{T_0}{T_g}, \pi_4 = \frac{E_h}{E_l}, \pi_5 = \frac{l_0}{d_0}$$
 (26)

where  $\hat{I}$  represents the competition between the heat generation and conduction, such that higher  $\hat{I}$  indicates heat generation is faster than conduction. The dimensionless number  $\hat{\alpha}$  is the ratio of the absorption decay length to the thickness, and larger  $\hat{a}$  indicates a larger light absorption region. The dimensionless number  $\hat{h}$  represents the competition between convection and conduction; higher  $\hat{h}$  indicates more heat loss than conduction. The dimensionless number g represents the amount of viscous relaxation of the SMP, while  $\varepsilon_{pre}$  represents the pre-stretch applied to the cantilever beam. The dimensionless number  $\pi_1$  represents the relation between the elastic energy and the thermal energy,  $\pi_2$  represents the competition between the relaxation time scale and conduction time scale,  $\pi_3$  is the ratio of the ambient to the glass transition temperatures,  $\pi_4$  is the ratio of the modulus under high temperature to low temperature, and  $\pi_5$  is the ratio of length to thickness. Note that the parameters  $C_1$  and  $C_2$  are not considered in the dimensionless numbers, since their values are fixed. Moreover, the length-to-width ratio  $\pi_5$  only influences the results of the two-dimensional FEA, but not the one-dimensional analytical model. The first five dimensionless numbers defined in equation (25) play more significant roles in governing the bending dynamics, and will be studied more carefully in the following. We set the same values for the parameters as in Section 2, so that the other dimensionless parameters are fixed as  $\pi_1$ 

 $0.33, \pi_2 = 0.0145, \pi_3 = 0.88, \ \pi_4 = 0.08$  and  $\pi_5 = 10$  without mentioning. For the studies about  $\hat{I}$ ,  $\hat{\alpha}$ , and  $\hat{h}$  in Section 4.1-4.3, we set g = 0.8 and  $\varepsilon_{pre} = 5\%$ . For the studies about g and  $\varepsilon_{pre}$  in Section 4.4 we set  $\hat{I} = 0.488, \ \hat{\alpha} = 0.06, \ \text{and} \ \hat{h} = 0.071.$ 

Meanwhile, we also obtain four time scales from dimensional analysis, which are:

$$t_1 = \frac{C_v d_0^2}{k}, t_2 = \frac{C_v \alpha T_0}{I_0}, t_3 = \frac{C_v d_0}{h}, t_4 = \frac{\eta}{E_I},$$
 (27)

where  $t_1$  is the time scale for conduction,  $t_2$  is the time scale for heat generation,  $t_3$  is the time scale for convection, and  $t_4$  is the time scale of viscous relaxation.  $t_1$  is used as the time scale to normalize the time in the following sections.

Next, we will study the effect of the five dimensionless numbers in equation (25) on the spatiotemporal behavior and bending dynamics of SMP beams. Since the results from the FEA and analytical model agree well with each other, we will only show the FEA results in this section.

### 4.1 Effect of $\hat{I}$

The spatiotemporal temperature of the SMP beam is affected significantly by the dimensionless parameter  $\hat{I}$ ; higher  $\hat{I}$  represents more heat generation compared to conduction. Due to photothermal heat generation, the surface temperature in a SMP beam monotonically increases with time (figure 9(a)). When  $\hat{I} \sim 1$ , the time for the surface temperature to reach  $T_g$  is comparable to  $t_1$ . As  $\hat{I}$  decreases, the temperature rises more slowly, and reaches  $T_g$  in a longer time. Figure 9(b) shows the temperature distributions through the thickness at  $t/t_1 = 2.5$ . A higher temperature gradient under higher  $\hat{I}$  (figure 9(b)) generates a higher strain gradient through the thickness of the beam, which induces a more significant bending (figure 9(c)). Higher  $\hat{I}$  also reduces the time to reach the maximum bending curvature,  $t_{max}$ , since the temperature in the entire sample reaches  $T_g$  faster. Figure 9(d) shows that as  $\hat{I}$  increases, the normalized maximum bending curvature of the beam,  $d_0/R_{max}$ , increases monotonically, and the normalized time to

reach the maximum bending curvature,  $t_{max}/t_1$ , decreases monotonically. When  $\hat{I}$  is low, for example,  $\hat{I}=0.325$  corresponding to  $I_0=2000$  Wm<sup>-2</sup> in figure 6, the bending curvature non-monotonically increases and decreases to a non-zero plateau value with time (see Supplementary video S1). When  $\hat{I}$  is even lower, for example,  $\hat{I}=0.284$  corresponding to  $I_0=1750$  Wm<sup>-2</sup> in figure 6, the bending curvature monotonically increases (see Supplementary video S1). These curves are not further shown here, since they have been shown in figure 6.

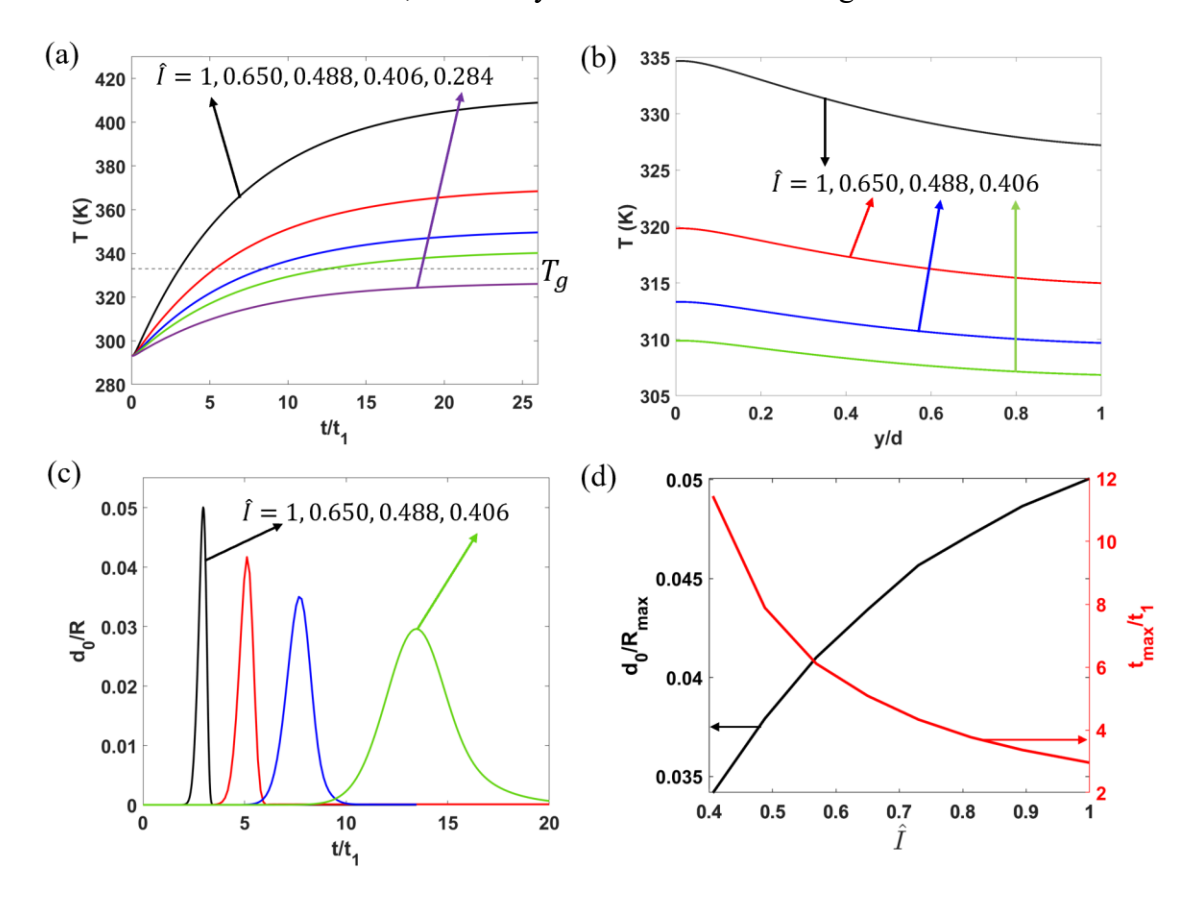


Figure 9 (a) Temporal evolution of the surface temperature of the cantilever beam for different  $\hat{I}=1,0.650,0.488,0.406,0.284$ . (b) Temperature distributions through the thickness at time  $t/t_1=2.5$ , and (c) temporal evolution of the bending curvature for different  $\hat{I}=1,0.650,0.488,0.406$ . (d) Dependence of the maximum bending curvature  $d_0/R_{max}$  and the time to reach the maximum bending curvature  $t_{max}/t_1$  on  $\hat{I}$ . Other dimensionless numbers are set as g=0.8,  $\varepsilon_{pre}=5\%$ ,  $\hat{\alpha}=0.06$ , and  $\hat{h}=0.071$ .

#### **4.2** Effect of $\hat{\alpha}$

The dimensionless parameters  $\hat{\alpha}$  describes the ratio of the absorption decay length to the thickness. As  $\hat{\alpha}$  increases, heat is generated in a larger region. When the absorption decay length is much greater than the beam thickness, heat is generated throughout the beam without much decay, so the temperature in the entire beam is distributed almost uniformly and reaches  $T_g$  rapidly, and the beam only bends slightly. At the other extreme, when the absorption decay length is much smaller than the beam thickness, heat is only generated in a thin surface layer of the SMP, which is not enough to trigger a significant bending of the beam even after a long time. Thus, the maximum bending curvature non-monotonically increases and then decreases with  $\hat{\alpha}$ , reaching an optimal value at around  $\hat{\alpha}=0.33$  (figure 10(a) and (b)). However, figure 10(b) shows that the time to reach the maximum bending curvature still decreases monotonically as  $\hat{\alpha}$  increases, since heat generation in a larger region takes shorter time of conduction for the entire beam to reach  $T_g$ .

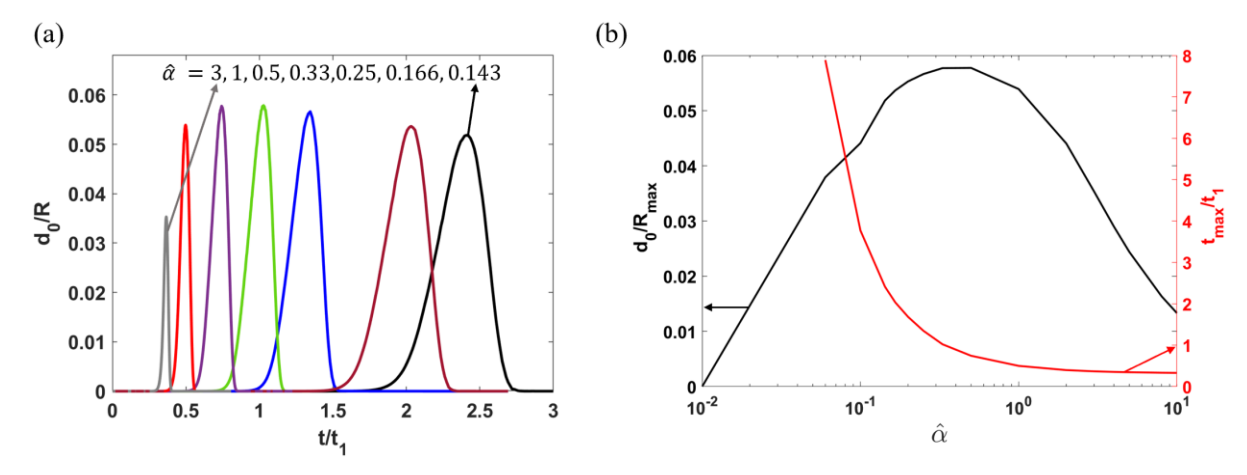


Figure 10 (a) Temporal evolution of the bending curvature for different  $\hat{\alpha}=3,1,0.5,0.33,0.25,0.166,0.143$ . (b) Dependence of the maximum bending curvature  $d_0/R_{max}$  and the time to reach the maximum bending curvature  $t_{max}/t_1$  on  $\hat{\alpha}$ . Other dimensionless numbers are set as g=0.8,  $\varepsilon_{pre}=5\%$ ,  $\hat{I}=0.488$ , and  $\hat{h}=0.071$ .

### 4.3 Effect of $\hat{h}$

Similar to  $\hat{I}$  and  $\hat{\alpha}$ , the dimensionless parameter  $\hat{h}$ , the competition between the heat loss and conduction, also influences the spatiotemporal temperature variation. Higher  $\hat{h}$  represents more heat loss on the boundary due to convection, resulting in a lower surface temperature. According to figure 6 and figure 9 (a), when  $\hat{I}=0.284$ , corresponding to  $I_0=1750~{\rm Wm}^{-2}$ , the temperature of the beam cannot reach  $T_g$  and the curvature increases monotonically. However, by decreasing the value of  $\hat{h}$  from 0.142, 0.071 to 0.035, the temperature of the beam can be controlled from below  $T_g$ , close to  $T_g$ , to above  $T_g$ , respectively (figure 11(a)). A lower  $\hat{h}$  generates a higher strain gradient and earlier bending with a higher curvature (figure 11(b)). Different types of bending behavior can also be achieved by tuning  $\hat{h}$  (figure 11(b)).

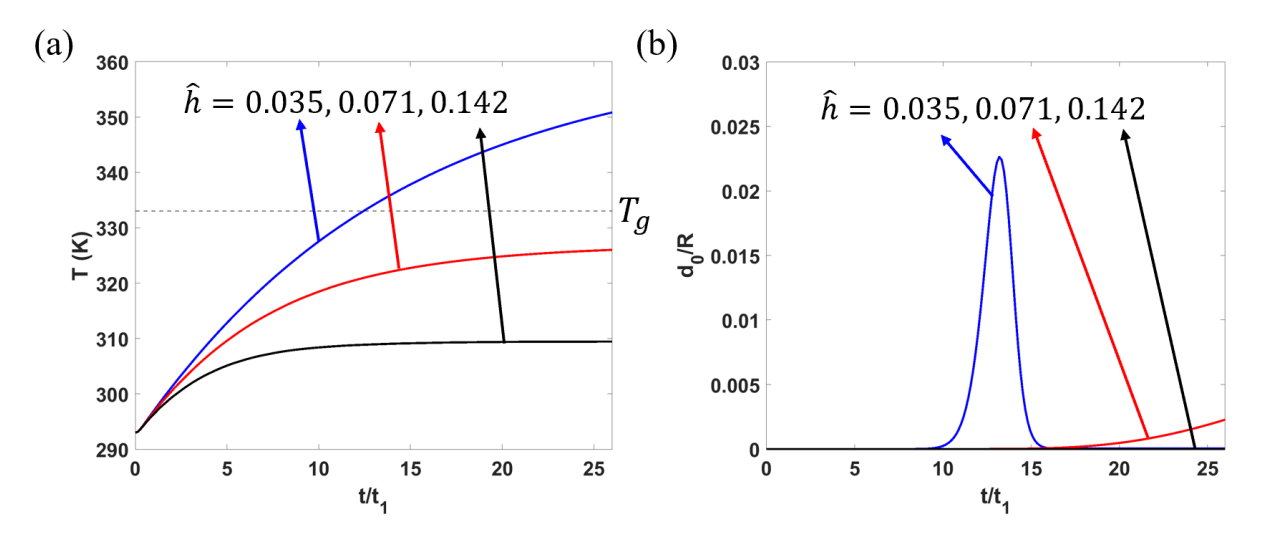


Figure 11 (a) Temporal evolution of the surface temperature, and (b) temporal evolution of the bending curvature for different  $\hat{h}=0.035,0.071,0.142$ . Other dimensionless numbers are set as  $g=0.8,~\varepsilon_{pre}=5\%,~\hat{l}=0.284,$  and  $\hat{\alpha}=0.06.$ 

### 4.4 Effect g and $\varepsilon_{pre}$

The dimensionless parameters g and  $\varepsilon_{pre}$ , which represent the amount of relaxation of the

material and the amount of pre-strain applied to the SMP, respectively, are two critical dimensionless parameters related to mechanical properties and loadings. Studies of g and  $\varepsilon_{pre}$ are conducted with fixed values of other dimensionless numbers,  $\hat{I} = 0.488$ ,  $\hat{\alpha} = 0.06$ , and  $\hat{h} = 0.06$ 0.071. We observe that both higher g and  $\varepsilon_{pre}$  lead to higher stored strain during recovery (figure 12(a) and (b)). Under the assumption of zero stress, the stored strain for a uniform contraction shown in figure 4 monotonically decreases when temperature and time increases. However, interestingly, for a SMP undergoing photothermally induced bending, we observe the stored strain  $\varepsilon_s$  at  $y/d_0 = 0$  non-monotonically decreases, increases and then decreases again with time for high  $\varepsilon_{pre} = 15\%$  (figure 12(b)). This is because the modulus and stored strain of the surface layer decrease dramatically when its temperature goes above  $T_g$ , while the temperature in the next layer can still be below  $T_g$ , leading to a large mismatch modulus and strain. This large mismatch modulus and strain can stretch the more compliant surface layer during bending, in conjunction with the heat transfer process, and cause non-monotonic changes of the stored strain. Moreover, we observe that both higher g and  $\varepsilon_{pre}$  lead to longer time to fully release the stored strain (figure 12(a) and (b)). As a result, the time to reach the maximum bending curvature,  $t_{max}/t_1$ , increases (figure 12(c)). However, compare to  $\varepsilon_{pre}$ , g influences  $t_{max}/t_1$  more significantly (figure 12(c)). Similarly, as g increases, the maximum bending curvature  $d_0/R_{max}$  increases under the same pre-strain  $\varepsilon_{pre}$  because the material stores more pre-stretch (figure 12(a) and (d)). On the other hand, if the viscoelastic relaxation g is fixed, the material stores more deformation with a higher pre-strain  $\varepsilon_{pre}$  (figure 12(b)), and therefore a higher maximum bending curvature  $d_0/R_{max}$  can also be achieved (figure 12(e)).

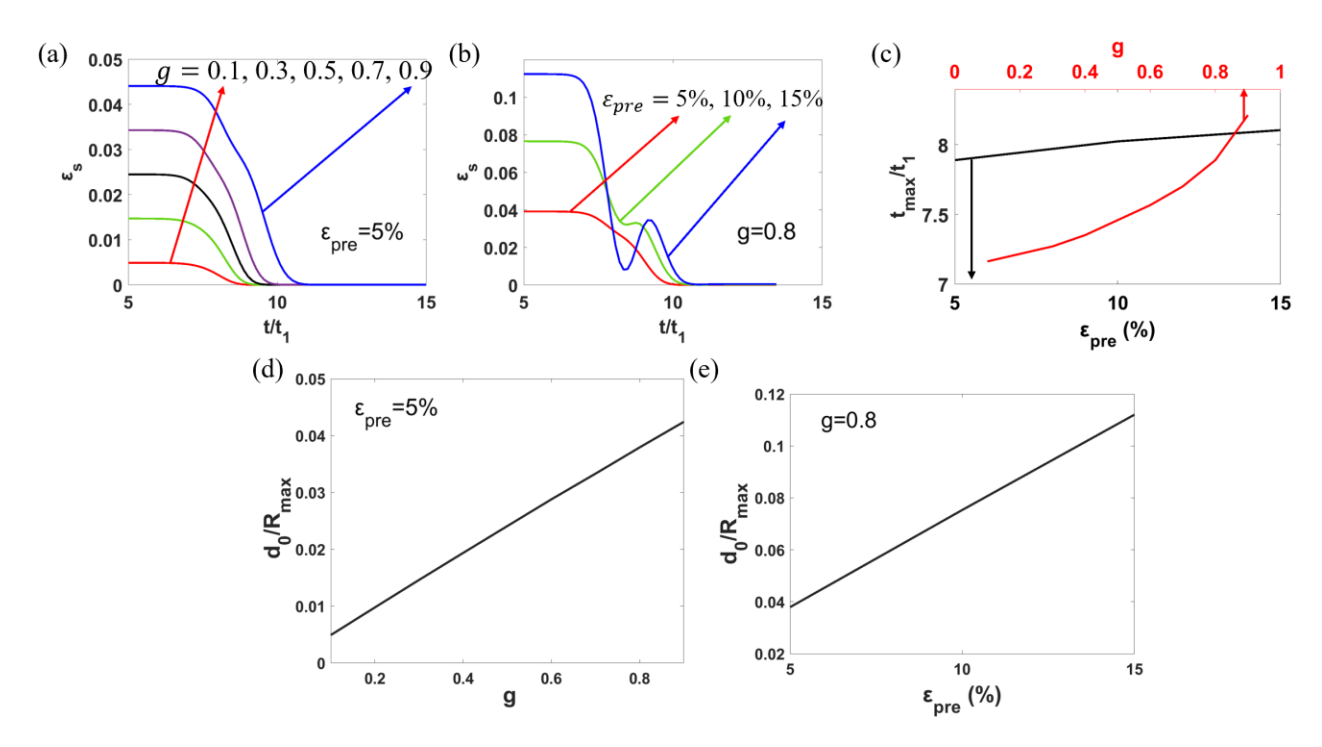


Figure 12 Temporal evolution of the stored strain (a) for different viscoelastic relaxation g=0.1, 0.3, 0.5, 0.7, 0.9 and (b) pre-strain  $\varepsilon_{pre}=5\%$ , 10%, 15% at  $y/d_0=0$ . (c) Time to reach the maximum bending curvature,  $t_{max}/t_1$ , as functions of g and  $\varepsilon_{pre}$ . Maximum bending curvature as functions of (d) g and (e)  $\varepsilon_{pre}$ . Other dimensionless numbers are set as  $\hat{I}=0.488$ ,  $\hat{\alpha}=0.06$ , and  $\hat{h}=0.071$ .

### 5 Changes in angles of incidence caused by deformation

When a SMP beam subjected to perpendicular illumination bends significantly, most parts are away from being perpendicular to the light incident, leading to reduced effective light intensity (figure 13). In this section, we include this effect of changes in angles of incidence caused by deformation into our analytical and finite element models, and investigate its influence on bending. In the previous FEA and analytical model in Section 2 and 3, the temperature field informs the distribution of the modulus and viscosity of the material to determine the deformation based on the prior loading history, whereas the deformation field does not affect the temperature field. Here

by accounting for changes in angles of incidence due to deformation, the deformation field can reversely alter the heat generation, making this a fully coupled problem.

We assume when the incident angle  $\theta$  is non-zero, the effective intensity of the incident light is  $I_0 \cos \theta$  [51], which describes the normal component of the light intensity  $I_0$ . We limit ourselves to an incident angle between  $0^\circ$  to  $90^\circ$ , since when the incident angle is more than  $90^\circ$ , the more complex self-shaded effect, i.e. the light source is blocked by the beam itself, has to be taken into consideration. We assume the angle of the incident light only influences the effective light intensity; the other kinetic processes, material properties, and geometry are the same as we discussed in the previous sections. In FEA, we define the incident angle  $\theta$  as the angle between the light and the normal direction of the top surface, which is a function of the x coordinate and time t,  $\theta = \theta(x, t)$  due to the spatiotemporal shape-morphing of the beam. The heat equation (10) can be rewritten as:

$$C_{\nu} \frac{\partial T}{\partial t} - k \frac{\partial^2 T}{\partial y^2} = \frac{I^*}{\alpha} e^{-\frac{y}{\alpha}},\tag{28}$$

where  $I^* = I_0 \cos(\theta(x, t))$ . To solve equation (28) by FEA, we develop a Python code to call ABAQUS CAE iteratively. In every iteration, we solve the displacement and the angle of incidence of every node, and update the heat generation by adding a new step into the CAE file and running the computation again to obtain the new angle of incidence (see Supplementary materials 2). To investigate the effect of changes in angles of incidence caused by deformation on the bending dynamics, we will next exam two cases: (1) perpendicular illumination ( $\theta_0 = 0^\circ$ , figure 14), and (2) tilted illumination (figure 15). For the studies in this section, we take  $\hat{I} = 0.488$ ,  $\hat{\alpha} = 0.06$ ,  $\hat{h} = 0.071$ , and g = 0.8 as the default values without mentioning.

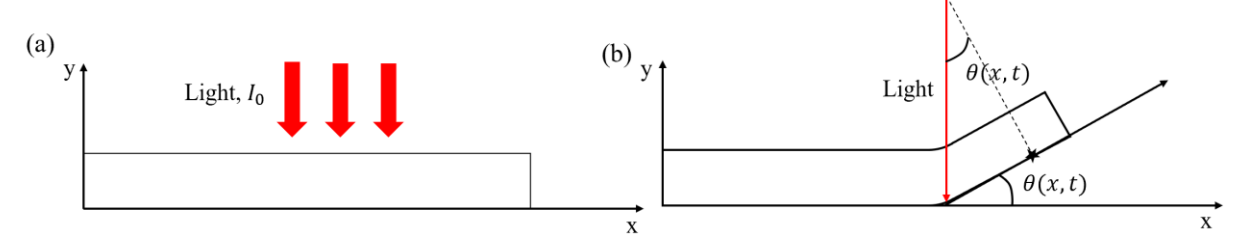


Figure 13 Schemetic of angle of incidence in the (a) initial configuration, and (b) bent configuration.

Here we take into consideration the effect of deformation on angle of incidence and model the bending dynamics of a SMP beam that is first uniaxially pre-stretched to 30%, fixed at a low temperature, and then subjected to perpendicular illumination (figure 14, see Supplementary video S2). When exposed to light, the beam bends significantly (figure 14(a)). As a result, most parts are far away from being perpendicular to the incident light, which reduces the effective light intensity in these regions and delays bending and unbending. Inhomogeneous curvature evolution from point A to point D is noticeable (figure 14(a)). At point A, which is close to the clamp end, the deflection, and therefore the incident angle, is small (figure 14(b)). As a result, the curvature of point A non-monotonically increases and then decreases to zero as time increases (figure 14(c)). As a comparison, the bending curvature of the case without changes in the angle of incidence, i.e. with a constant zero angle of incidence, is also plotted, and called the reference (the blue curve in figure 14(c)). Since the bending curvature of the reference case is uniform, the result is the same no matter what point is considered. The evolution of the bending curvature of point A is similar to the reference case, but shows a slightly lower maximum bending curvature at a later time since the angle of incident light slightly reduces the light intensity. The beam at point B has a larger bending angle (figure 14(b)), so the curvature of point B initially increases in the same manner as that of point A, then remains at a non-zero plateau value for certain time, and finally decreases to zero (figure 14(c)). As compared with that of the previous points, the bending angles at points C and D are much higher (figure 14(b)). Correspondingly, the curvatures of points C and D first increase, remain at a non-zero plateau, then increase again to the maximum curvature, and finally decrease to zero (figure 14(c)). This means that the beam first partially bends at the two points, then continues the bending after a delay time, and finally unbends. The plateau curvature of point D is lower but lasts longer than that of point C due to the greater bending angle of point D. In summary, complex and inhomogeneous curvature evolution is observed at different points. As a result, the dimensionless deflection at the tip  $x = l_0$ ,  $V(l_0)/l_0$ , reaches a maximum value at a later time than that of the reference case with a constant zero angle of incidence due to reduced effective light intensity (figure 14(d)). However, the maximum deflection of the reference is slightly lower,

because the bending is slightly over 90°, which is supposed to be corrected for the self-shaded effect.

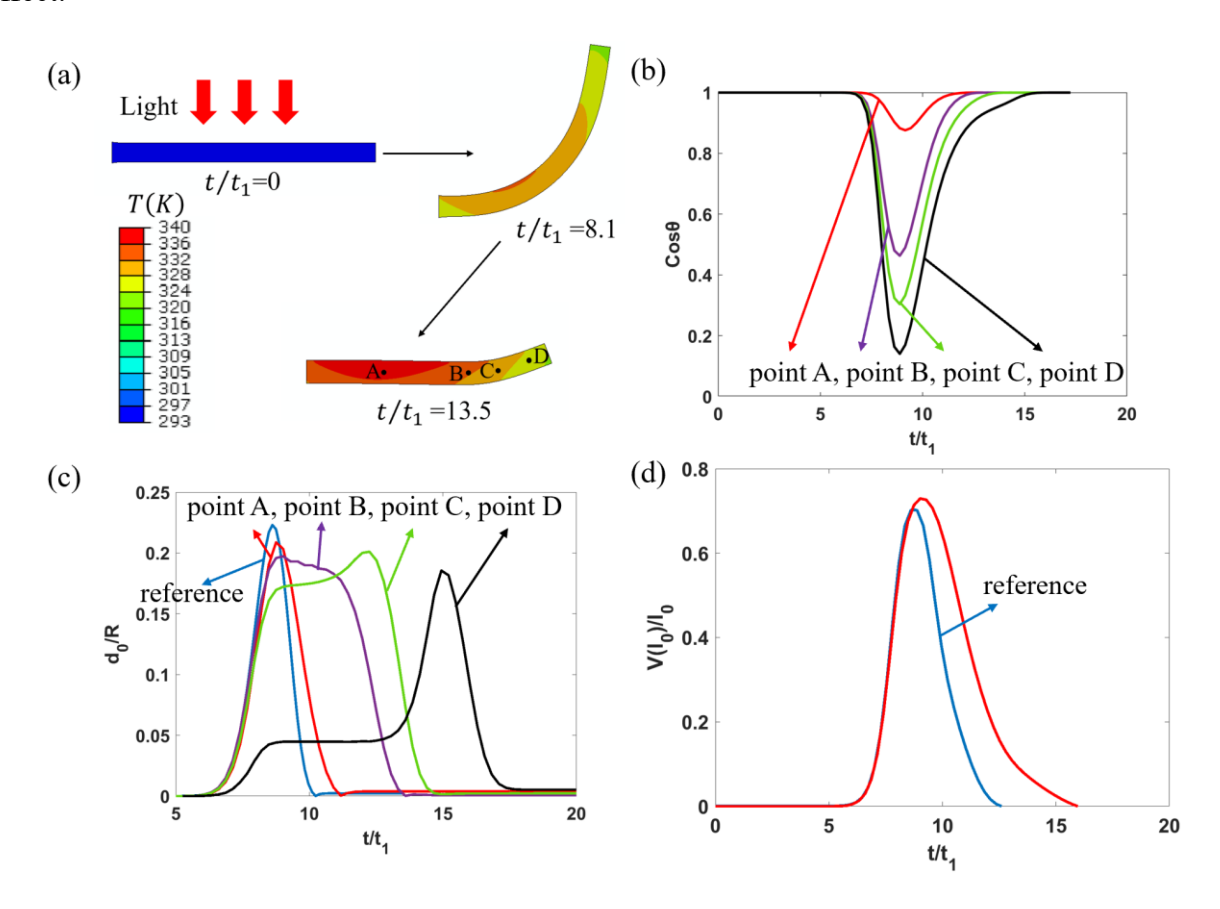


Figure 14 Effect of changes in angles of incidence caused by deformation on bending dynamics for a SMP beam subjected to perpendicular illumination. (a) FEA result of the shape evolution of a SMP beam which is first pre-stretched to 30%, and then subjected to perpendicular light illumination. The three contour plots show the shape and temperature distribution at  $t/t_1 = 0$ , 8.1, 13.5, respectively. Temporal evolution of (b)  $\cos\theta$  and (c) bending curvature  $d_0/R$  at different points  $x/l_0 = 0.32$ , 0.64, 0.76, 0.92 defined in part a, with the reference curve showing the behavior of a constant zero angle of incidence of the homogeneous bending of a SMP beam. (d) Temporal evolution of the dimensionless tip deflection,  $V(l_0)/l_0$ .

Next, we model the bending dynamics of a SMP beam that is first pre-stretched to 30%, and then subjected to tilted illumination at an initial incident angle of 30° (figure 15, see Supplementary

video S2). In some regions, the bending causes the incident angle to non-monotonically decrease to zero, and then increase again (figure 15(b)). Due to the non-monotonic changes of the angle of incidence, it is expected that the effect of changes in angles of incidence plays a less significant role on the average bending dynamics in this case of the tilted illumination than that in the perpendicular illumination. Even though, different types of temporal evolution of curvature are still observed at different locations (figure 15(c)). Point A is close to the clamp end, so the angle of incidence becomes larger than the initial angle  $\theta_0$  at all time. Therefore, the curvature of point A non-monotonically increases and decreases to zero, where the maximum curvature is reached earlier than that in the reference case with a constant incident angle  $\theta_0$ , although later than that in the reference case with a constant zero incident angle (figure 15(c)); the bending curvatures of both reference cases are uniform. The bending angle of point B is larger, so the angle of incidence non-monotonically decreases to zero, and then increases to above  $\theta_0$  (figure 15(b)). Although the curvature at point B still non-monotonically increases and decreases to zero, there is a slight delay compared to the reference case with a constant incident angle  $\theta_0$  (figure 15(c)). Further away from the clamp end, point C reaches a higher angle of incidence due to bending after the nonmonotonic change (figure 15(b)), and has more obvious delay in bending (figure 15(c)). Nevertheless, in comparison to the perpendicular illumination, this case of tilted illumination is less influenced by changes in the angles of incidence, and does not show complex temporal bending behavior in some regions, like partial bending and continued bending after a delay time. As a result of the non-monotonic decrease and increase of the angle of incidence, the dimensionless tip deflection,  $V(l_0)/l_0$ , reaches a lower maximum value but at an earlier time, compared to the reference case with a constant angle of incidence  $\theta_0$  (figure 15(d)).

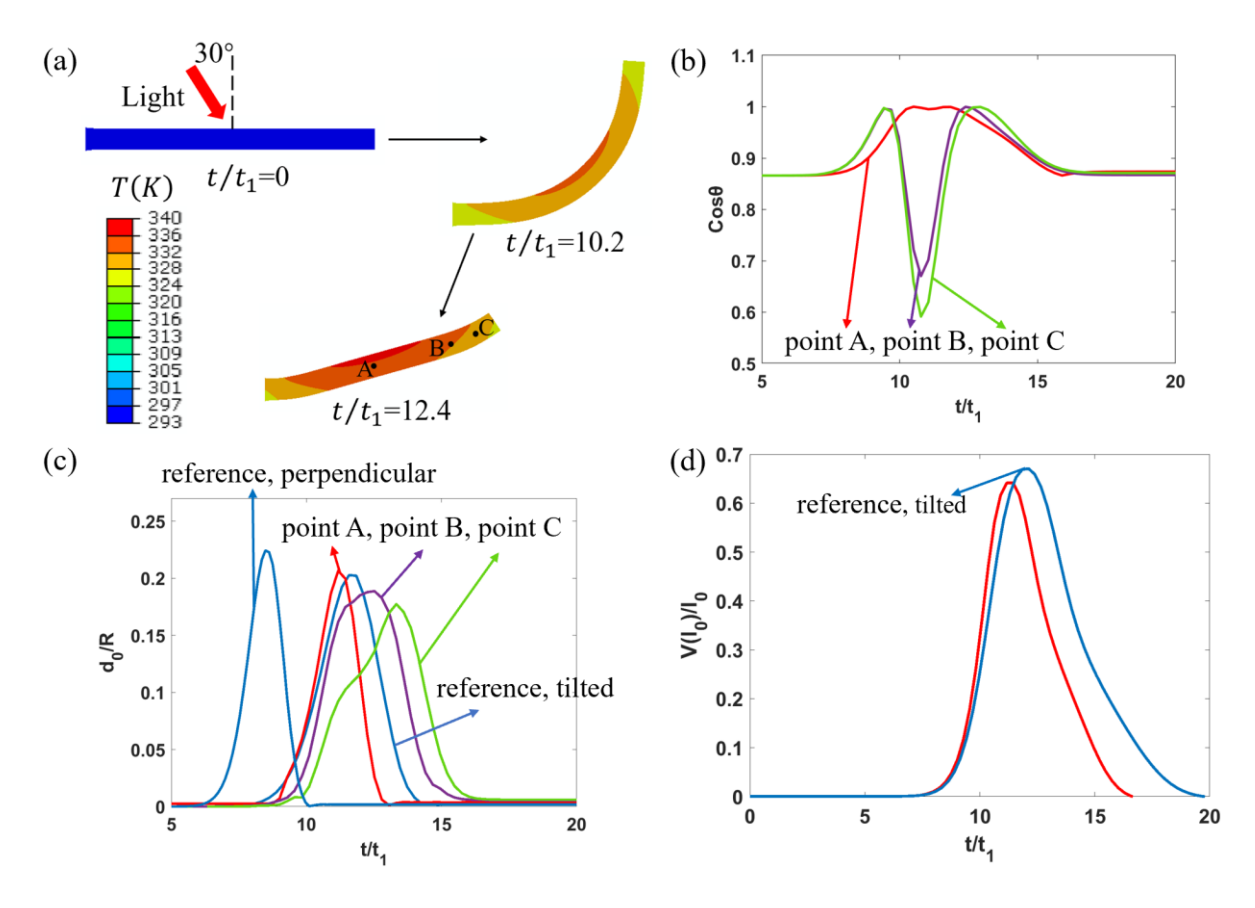


Figure 15 Effect of changes in angles of incidence caused by deformation on bending dynamics for a SMP beam subjected to tilted illumination. (a) FEA results of the shape evolution of a SMP beam which is first pre-stretched to 30%, and then subjected to 30° light illumination. The three contour plots show the shape and temperature distribution at  $t/t_1 = 0$ , 10.2, 12.4, respectively. Temporal evolution of (b)  $\cos\theta$  and (c) bending curvature at different points  $x/l_0 = 0.44$ , 0.85, 0.93 defined in part a, with the reference curve showing the behavior of constant zero and constant 30° angles of incidence of the homogeneous bending of a SMP beam. (d) Temporal evolution of the dimensionless tip deflection,  $V(l_0)/l_0$ .

## **6** Experiments

To experimentally validate our theoretical predictions of the spatiotemporal shape-morphing

of SMPs, epoxy-based SMPs are prepared by mixing the epoxy monomer D.E.R. 362 (Olin, molecular weight  $\sim 398~g~mol^{-1}$  and epoxy equivalent weight 199  $g~mol^{-1}$ ) and the curing agent Jeffamine D230 (Sigma Aldrich) with a ratio of 1.25 : 1, which gives rise to a relatively low glass transition temperature at 50 °C (figure 16(a)) and a high elongation up to 70% [52]. Subsequently, 0.1 wt % reduced graphene oxide (RGO) (Xfnano) is dispersed into the precursor, which enables the photothermal ability of the polymer. Then the precursor is vacuumed to remove air bubbles and cast into a flat petri-dish for thermal curing at 80 °C for five hours. After curing, a 40 mm  $\times$  10 mm  $\times$  1.5 mm sample is cut from the original sample (figure 16(b)).

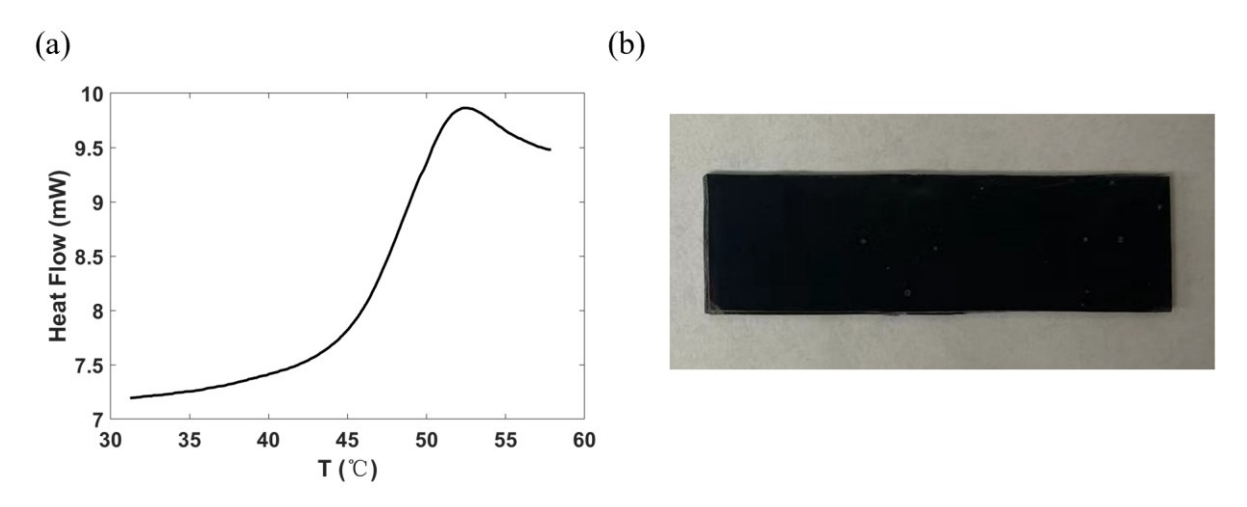


Figure 16 (a) Differential scanning calorimetry (DSC) results for the epoxy SMP. (b) A typical rectangular sample.

The sample is first heated and subjected to a pre-strain of 20% using a stretcher. Then the sample is cooled to the room temperature prior to removing the load to store the pre-stretch. Next, the sample is clamped at one end, illuminated perpendicularly by an infrared heat light (Westinghouse Lighting R40) to trigger spatiotemporal recovery. To achieve different bending dynamics, we change the distance between the light source and beam surface to vary the light intensity, i.e. the dimensionless number  $\hat{I}$  (figure 17(a)-(d), see Supplementary video S3). When  $\hat{I}$  is extremely low, the beam never bends (figure 17(a)). When  $\hat{I}$  is slightly higher, the bending curvature slowly but monotonically increases (figure 17(b)). When  $\hat{I}$  becomes even higher, the

beam first bends, reaching the maximum bending curvature, and then unbends to a non-zero plateau curvature (figure 17(c)). When  $\hat{I}$  is high enough, the bending curvature non-monotonically increases and then decreases to zero, completely recovering the initial shape (figure 17(d)).

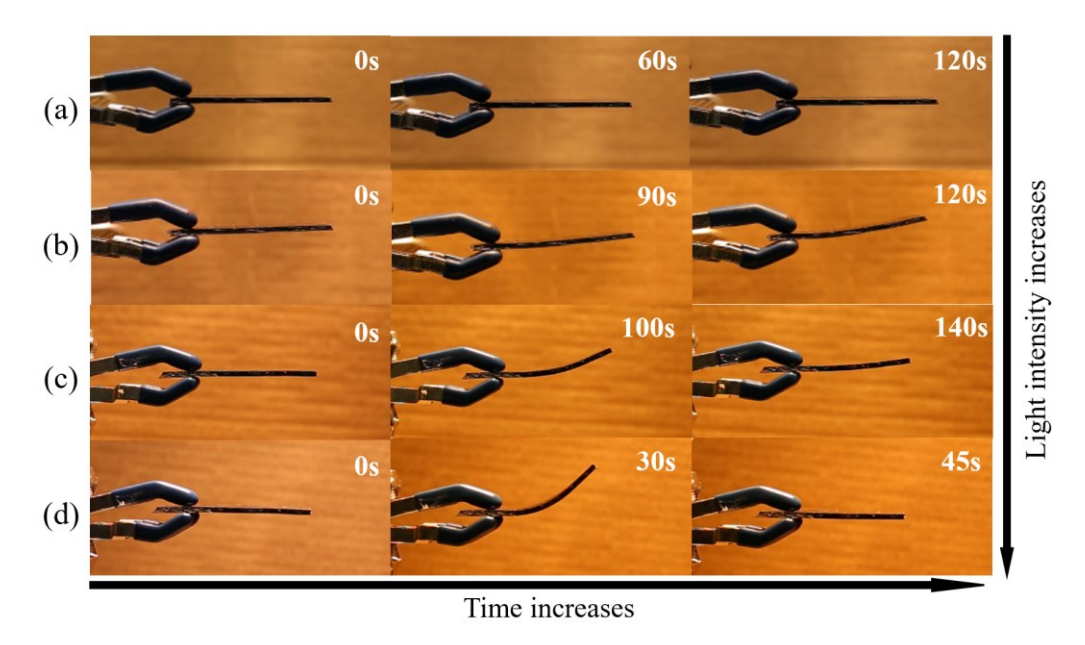


Figure 17 Snapshots in temporal sequences showing different types of bending dynamics of a SMP cantilever beam with 20% pre-strain as  $\hat{I}$  increases: (a) no bending, (b) bending to a constant curvature, (c) bending and unbending to a non-zero curvature, and (d) bending and unbending to a zero curvature.

Next, we applied a large pre-strain of 30% to a SMP to obtain significant bending under perpendicular illumination, and demonstrate the effect of changes in angles of incidence caused by deformation on the bending dynamics (figure 18, see Supplementary video S4). At t = 30 s, most parts of the beam are away from being perpendicular to the incident light, which minimizes the effective light intensity in this region. As a result, the bending-unbending process has a significant delay. Changing in the bent shape from t = 30 s to t = 50 s is slow until most parts of the beam are back to being perpendicular to the incident light. Eventually, at around t = 80 s, the

beam recovers its initial state, much slower than the ones with a lower pre-stretch under the same light intensity (figure 17(d)).

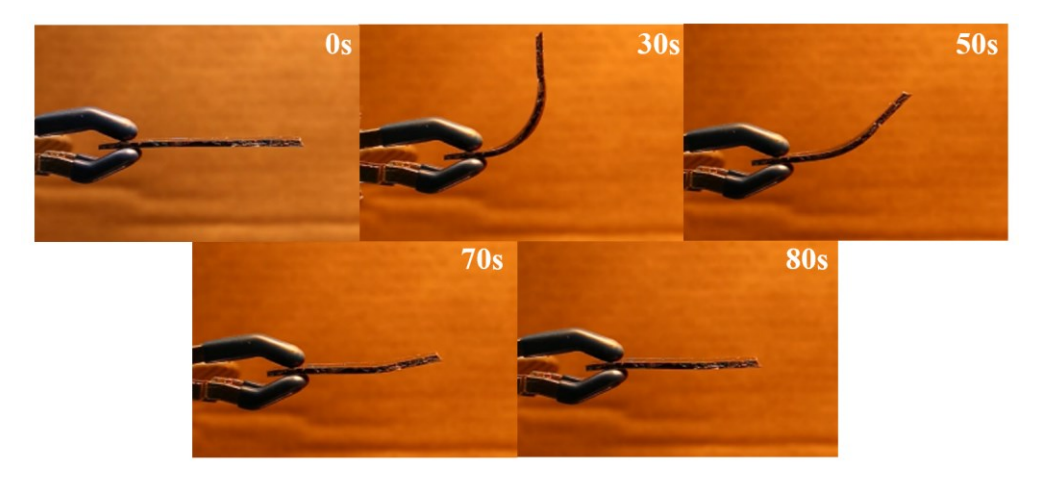


Figure 18 Snapshots in a temporal sequence showing a delay of the bending dynamics of a SMP beam with 30% pre-strain attributed to the effect of changes in angles of incidence caused by large bending.

### 7 Conclusion

In conclusion, this paper investigates the spatiotemporal responses of photothermal SMPs through multiple non-equilibrium kinetic processes by combining FEA, analytical modeling, and experiments. We consider a full thermomechanical cycle of a photothermal SMP beam, where it is first pre-stretched at a high temperature, cooled down to a low temperature prior to removing the load, and subsequently illuminated by a light for shape recovery. In the recovery step, we model the multiple non-equilibrium processes in the SMP, including heat generation, conduction and viscoelastic relaxation, to predict its spatiotemporal responses. The non-equilibrium processes can induce highly inhomogeneous temperature and strain distributions through the thickness, and therefore trigger bending, and even unbending of the beam. Our dimensional analysis shows that the key dimensionless numbers, mainly involving the multiple kinetic constants, geometric

parameters, and thermomechanical loading conditions, govern the spatiotemporal responses. By systematically varying the key dimensional parameters, we observe three different types of bending behaviors: (1) the beam can monotonically bend to a constant curvature, (2) bend and unbend to a non-zero curvature, or (3) bend and unbend to a zero curvature. Experimentally, we characterize the spatiotemporal recovery of SMP beams after a similar thermomechanical loading cycle, and observe different types of bending dynamics, which agree well with those predicted by the theory. Furthermore, the effect of changes in angles of incidence caused by extensive bending is carefully investigated by FEA and validated by experiments. This work identifies that the concurrent heat transfer and viscoelastic relaxation processes govern the spatiotemporal responses of photothermal SMPs, and demonstrates a generic method of studying the spatiotemporal behavior of SRSMs governed by multiple non-equilibrium processes, which provides design guidelines for spatiotemporal morphing structures and robots.

In the future, our theoretical and experimental work can be improved in a few aspects. First, the current material model of SMPs is simple, and a more sophisticated and thermodynamically consistent model could be considered [53,54]. Second, we only qualitatively validate the spatiotemporal responses of photothermal SMPs in the experiments in this paper. Quantitative comparison between experiments and theory will be conducted in the future, which however, will require careful measurements of the photothermal and mechanical properties of SMPs.

## Acknowledgement

This work is supported by National Science Foundation through a CAREER Award No. CMMI-2048219. This work used computational and storage services associated with the Hoffman2 Shared Cluster provided by Institute for Digital Research and Education's Research Technology Group at the University of California, Los Angeles (UCLA). The authors acknowledge the helpful discussions with Laurent Pilon and Yu Zhou at UCLA.

### Reference

- 1. Hu L, Wan Y, Zhang Q, Serpe MJ. Harnessing the power of stimuli-responsive polymers for actuation. Advanced Functional Materials. 2020 Jan;30(2):1903471.
- Stuart MA, Huck WT, Genzer J, Müller M, Ober C, Stamm M, Sukhorukov GB, Szleifer I, Tsukruk VV, Urban M, Winnik F. Emerging applications of stimuli-responsive polymer materials. Nature materials. 2010 Feb;9(2):101-13.
- 3. Ionov L. Polymeric actuators. Langmuir. 2015 May 12;31(18):5015-24.
- 4. Meng H, Li G. A review of stimuli-responsive shape memory polymer composites. polymer. 2013 Apr 19:54(9):2199-221.
- 5. Mather PT, Luo X, Rousseau IA. Shape memory polymer research. Annual Review of Materials Research. 2009 Aug 4;39(1):445-71.
- 6. Zhao Q, Qi HJ, Xie T. Recent progress in shape memory polymer: New behavior, enabling materials, and mechanistic understanding. Progress in Polymer Science. 2015 Oct 1;49:79-120.
- 7. Kim H, Ahn SK, Mackie DM, Kwon J, Kim SH, Choi C, Moon YH, Lee HB, Ko SH. Shape morphing smart 3D actuator materials for micro soft robot. Materials Today. 2020 Dec 1;41:243-69.
- 8. Li C, Iscen A, Palmer LC, Schatz GC, Stupp SI. Light-driven expansion of spiropyran hydrogels. Journal of the American Chemical Society. 2020 Apr 24;142(18):8447-53.
- 9. Ahn SK, Kasi RM, Kim SC, Sharma N, Zhou Y. Stimuli-responsive polymer gels. Soft Matter. 2008;4(6):1151-7.
- 10. Osada Y, Gong JP. Soft and wet materials: polymer gels. Advanced materials. 1998 Aug;10(11):827-37.
- 11. Lendlein A, Langer R. Biodegradable, elastic shape-memory polymers for potential biomedical applications. Science. 2002 May 31;296(5573):1673-6.
- 12. Huang Y, Zhu M, Huang Y, Pei Z, Li H, Wang Z, Xue Q, Zhi C. Multifunctional energy storage and conversion devices. Advanced Materials. 2016 Oct;28(38):8344-64.
- 13. Wang X, Dong L, Zhang H, Yu R, Pan C, Wang ZL. Recent progress in electronic skin. Advanced Science. 2015 Oct;2(10):1500169.
- 14. Yu Y, Peng R, Chen Z, Yu L, Li J, Wang J, Liu X, Wang Q, Wang X. Photoresponsive Biomimetic Soft Robots Enabled by Near-Infrared-Driven and Ultrarobust Sandwich-Structured Nanocomposite Films. Advanced Intelligent Systems. 2021 Sep;3(9):2100012.
- 15. Lee Y, Song WJ, Sun JY. Hydrogel soft robotics. Materials Today Physics. 2020 Dec 1;15:100258.
- 16. Srivastava V, Chester SA, Anand L. Thermally actuated shape-memory polymers: Experiments, theory, and numerical simulations. Journal of the Mechanics and Physics of Solids. 2010 Aug 1;58(8):1100-24.
- 17. Rousseau IA. Challenges of shape memory polymers: A review of the progress toward overcoming SMP's limitations. Polymer Engineering & Science. 2008 Nov;48(11):2075-89.
- 18. Guo F, Zheng X, Liang C, Jiang Y, Xu Z, Jiao Z, Liu Y, Wang HT, Sun H, Ma L, Gao W. Millisecond response of shape memory polymer nanocomposite aerogel powered by stretchable graphene framework. ACS nano. 2019 Apr 23;13(5):5549-58.
- 19. Xuan C, Jin L. Concurrent reaction and diffusion in photo-responsive hydrogels. Journal of the Mechanics and Physics of Solids. 2019 Mar 1;124:599-611.

- 20. Satoh T, Sumaru K, Takagi T, Kanamori T. Fast-reversible light-driven hydrogels consisting of spirobenzopyran-functionalized poly (N-isopropylacrylamide). Soft Matter. 2011;7(18):8030-4.
- Qian X, Zhao Y, Alsaid Y, Wang X, Hua M, Galy T, Gopalakrishna H, Yang Y, Cui J, Liu N, Marszewski M. Artificial phototropism for omnidirectional tracking and harvesting of light. Nature nanotechnology. 2019 Nov;14(11):1048-55.
- 22. Zhou Y, Jin L. Hydrolysis-induced large swelling of polyacrylamide hydrogels. Soft Matter. 2020;16(24):5740-9.
- 23. Hon KK, Corbett D, Terentjev EM. Thermal diffusion and bending kinetics in nematic elastomer cantilever. The European Physical Journal E. 2008 Jan;25(1):83-9.
- 24. Korner K, Kuenstler AS, Hayward RC, Audoly B, Bhattacharya K. A nonlinear beam model of photomotile structures. Proceedings of the National Academy of Sciences. 2020 May 5;117(18):9762-70.
- 25. Reyssat E, Mahadevan L. How wet paper curls. EPL (Europhysics Letters). 2011 Mar 10;93(5):54001.
- Ma M, Guo L, Anderson DG, Langer R. Bio-inspired polymer composite actuator and generator driven by water gradients. Science. 2013 Jan 11;339(6116):186-9.
- 27. Treml BE, McKenzie RN, Buskohl P, Wang D, Kuhn M, Tan LS, Vaia RA. Autonomous motility of polymer films. Advanced Materials. 2018 Feb;30(7):1705616.
- 28. Douezan S, Wyart M, Brochard-Wyart F, Cuvelier D. Curling instability induced by swelling. Soft Matter. 2011;7(4):1506-11.
- 29. Maeda S, Hara Y, Sakai T, Yoshida R, Hashimoto S. Self-walking gel. Advanced Materials. 2007 Nov 5:19(21):3480-4.
- 30. Yoshida R, Takahashi T, Yamaguchi T, Ichijo H. Self-oscillating gels.
- 31. Mao Y, Yu K, Isakov MS, Wu J, Dunn ML, Jerry Qi H. Sequential self-folding structures by 3D printed digital shape memory polymers. Scientific reports. 2015 Sep 8;5(1):1-2.
- 32. Liu Y, Shaw B, Dickey MD, Genzer J. Sequential self-folding of polymer sheets. Science Advances. 2017 Mar 3:3(3):e1602417.
- 33. Liu Y, Boyles JK, Genzer J, Dickey MD. Self-folding of polymer sheets using local light absorption. Soft matter. 2012;8(6):1764-9.
- 34. Chen T, Bilal OR, Shea K, Daraio C. Harnessing bistability for directional propulsion of soft, untethered robots. Proceedings of the National Academy of Sciences. 2018 May 29;115(22):5698-702.
- 35. Guseinov R, McMahan C, Pérez J, Daraio C, Bickel B. Programming temporal morphing of self-actuated shells. Nature communications. 2020 Jan 13;11(1):1-7.
- 36. Waters JT, Li S, Yao Y, Lerch MM, Aizenberg M, Aizenberg J, Balazs AC. Twist again: Dynamically and reversibly controllable chirality in liquid crystalline elastomer microposts. Science advances. 2020 Mar 27;6(13):eaay5349.
- 37. Li S, Lerch MM, Waters JT, Deng B, Martens RS, Yao Y, Kim DY, Bertoldi K, Grinthal A, Balazs AC, Aizenberg J. Self-regulated non-reciprocal motions in single-material microstructures. Nature. 2022 May;605(7908):76-83.
- 38. Xuan C, Zhou Y, Zhao Y, He X, Jin L. Photodriven Self-Excited Hydrogel Oscillators. Physical Review Applied. 2022 Jan 6;17(1):014007.
- 39. Ding Z, Yuan C, Peng X, Wang T, Qi HJ, Dunn ML. Direct 4D printing via active composite materials. Science advances. 2017 Apr 12;3(4):e1602890.
- 40. Peng W, Zhang G, Zhao Q, Xie T. Autonomous Off-Equilibrium Morphing Pathways of a Supramolecular Shape-

- Memory Polymer. Advanced Materials. 2021 Aug;33(34):2102473.
- 41. Kuang X, Roach DJ, Wu J, Hamel CM, Ding Z, Wang T, Dunn ML, Qi HJ. Advances in 4D printing: materials and applications. Advanced Functional Materials. 2019 Jan;29(2):1805290.
- 42. Torras N, Zinoviev KE, Marshall JE, Terentjev EM, Esteve J. Bending kinetics of a photo-actuating nematic elastomer cantilever. Applied physics letters. 2011 Dec 19;99(25):254102.
- 43. Li M, Lv S, Zhou J. Photo-thermo-mechanically actuated bending and snapping kinetics of liquid crystal elastomer cantilever. Smart materials and structures. 2014 Oct 27;23(12):125012.
- 44. Mu X, Sowan N, Tumbic JA, Bowman CN, Mather PT, Qi HJ. Photo-induced bending in a light-activated polymer laminated composite. Soft Matter. 2015;11(13):2673-82.
- 45. Takaffoli M, Zhang T, Parks D, Zhao X. Mechanochemically responsive viscoelastic elastomers. Journal of Applied Mechanics. 2016 Jul 1;83(7).
- 46. Wang QM, Mohan AC, Oyen ML, Zhao XH. Separating viscoelasticity and poroelasticity of gels with different length and time scales. Acta Mechanica Sinica. 2014 Feb;30(1):20-7.
- 47. Tobushi H, Hashimoto T, Hayashi S, Yamada E. Thermomechanical constitutive modeling in shape memory polymer of polyurethane series. Journal of intelligent material systems and structures. 1997 Aug;8(8):711-8.
- 48. Al Azzawi W, Epaarachchi JA, Islam M, Leng J. Implementation of a finite element analysis procedure for structural analysis of shape memory behaviour of fibre reinforced shape memory polymer composites. Smart Materials and Structures. 2017 Oct 30;26(12):125002.
- 49. Williams ML, Landel RF, Ferry JD. The temperature dependence of relaxation mechanisms in amorphous polymers and other glass-forming liquids. Journal of the American Chemical society. 1955 Jul;77(14):3701-7.
- 50. Jin L, Jiang X, Huo Y. Light-induced nonhomogeneity and gradient bending in photochromic liquid crystal elastomers. Science in China Series G: Physics, Mechanics and Astronomy. 2006 Oct;49(5):553-63.
- 51. Corbett D, Xuan C, Warner M. Deep optical penetration dynamics in photobending. Physical Review E. 2015 Jul 31;92(1):013206.
- 52. Zheng N, Fang G, Cao Z, Zhao Q, Xie T. High strain epoxy shape memory polymer. Polymer Chemistry. 2015;6(16):3046-53.
- 53. Huang R, Zheng S, Liu Z, Ng TY. Recent advances of the constitutive models of smart materials—Hydrogels and shape memory polymers. International Journal of Applied Mechanics. 2020 Mar 23;12(02):2050014.
- 54. Nguyen TD. Modeling shape-memory behavior of polymers. Polymer Reviews. 2013 Jan 1;53(1):130-52.